Materials & Design 238 (2024) 112690

Contents lists available at ScienceDirect

Materials & Design

journal homepage: www.elsevier.com/locate/matdes

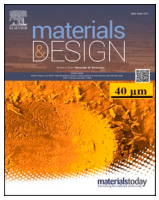

Ex-situ characterization and simulation of density fluctuations evolution during sintering of binder jetted 316L

Alberto Cabo Rios [a,b,*], Tatiana Mishurova [c], Laura Cordova [a], Mats Persson [d], Giovanni Bruno [c,e], Eugene Olevsky [b,f], Eduard Hryha [a]

[a] Chalmers University of Technology, Industrial and Materials Science, Göteborg, Sweden
[b] Mechanical Engineering, San Diego State University, San Diego, USA
[c] Bundesanstalt für Materialforschung und–prüfung (BAM), Unter den Eichen 87, Berlin 12205, Germany
[d] Digital Metal AB, Höganäs, Sweden
[e] Institute of Physics and Astronomy, University of Potsdam, Karl-Liebknecht-Straße 24-25, Potsdam 14476, Germany
[f] NanoEngineering, University of California, San Diego, La Jolla, USA

ARTICLE INFO

Keywords:
Additive manufacturing
Synchrotron X-Ray CT
Binder Jetting
Sintering
FEM simulation

ABSTRACT

Efficient density evolution during sintering of the as-printed component is vital to reach full densification and required properties of binder jet (BJT) components. However, due to the high porosity and brittle nature of the green compact, analysis of the microstructure development during sintering is very difficult, resulting in lack of understanding of the densification process. Density development from green state (57 ± 1.6 %) up to full density (99 ± 0.3 %) was characterized by high-resolution synchrotron X-Ray computed tomography (SXCT) on BJT 316L samples from ex-situ interrupted sintering tests. Periodicity of density fluctuations along the building direction was revealed for the first time and was related to the layer thickness of ~ 42 μm during printing that decreased down to ~ 33 μm during sintering. Sintering simulations, utilizing a continuum sintering model developed for BJT, allowed to replicate the density evolution during sintering with a mean error of 2 % and its fluctuation evolution from green (1.66 %) to sintered (0.56 %) state. Additionally, simulation of extreme particle size segregation (1 μm to 130 μm) suggested that non-optimized printing could lead to undesirable density fluctuation amplitude rapid increase (~10 %) during sintering. This might trigger the nucleation of defects (e.g., layer delamination, cracking, or excessive residual porosity) during the sintering process.

1. Introduction

Metal binder jetting (BJT) is a multi-step additive manufacturing (AM) process in which the component is shaped by the printing step and the final properties of the material are achieved by a second sintering step (when components is typically exposed to the temperatures in the range of 75 to 95 % of the powder material melting point, sometimes even higher but below the melting point of the powder material). This new generation of AM manufacturing process has several benefits compared with traditional subtractive manufacturing. In general, the ability of manufacturing highly complex component geometries or to redesign and manufacture and assembly of part as one AM component are some of the advantages. Moreover, insignificant material waste is produced when just the required powder material is used to produce a specific component. Specifically, the non-thermal BJT printing has minor/limited effect on the powder within the powder bed, avoiding most of the powder reusability issues more common in other metal AM processes.

Typically, porosity in the final components is an unwanted outcome of the BJT manufacturing process and, in general, AM technologies. However, depending on the intended application, some level of porosity may be desired within the final component. For instance, some porous structures are desirable for medical applications [1], porous filters [2–4] or battery components [5]. On the contrary, structural components for automotive [6] or aerospace [7] applications require the highest level of mechanical properties possible and therefore minimal porosity. This requires achieving higher densification at the end of the sintering process and certain microstructural properties (e.g., grain size, phase composition, size and shape of residual porosity). Therefore, a predictive tool is needed to reproduce the detailed evolution of the complete sintering process from the initial green compact until the very end of the

* Corresponding author at: Department of Industrial and Materials Science, Chalmers University of Technology, Rännvägen 2A, Gothenburg 412 96, Sweden.
E-mail address: cabo@chalmers.se (A. Cabo Rios).

https://doi.org/10.1016/j.matdes.2024.112690
Received 23 October 2023; Received in revised form 17 January 2024; Accepted 19 January 2024
Available online 20 January 2024

Nomenclature

F	Free energy (J)
V	Pore Volume (m^3)
S	Pore surface area (m^2)
K	Effective bulk viscosity $(Pa \bullet s)$
ρ	Relative density
θ	Porosity
σ_{ij}	Stress tensor $(N \bullet m^{-2})$
$\dot{\varepsilon}_{ij}$	Strain rate tensor (s^{-1})
$\dot{e}$	Trace of the strain rate tensor (s^{-1})
δ_{ij}	Delta de Kronecker
φ	Normalized shear modulus
ψ	Normalized bulk modulus
P_L	Effective sintering stress (Pa)
α	Surface energy $(J \bullet m^{-2})$
η_0	Material viscosity $(Pa \bullet s)$
A_1	Viscosity pre-exponential factor below $T_T (Pa \bullet s \bullet K^{-1})$
Q_1	Viscosity activation energy below $T_T (J \bullet mol^{-1})$
A_2	Viscosity pre-exponential factor above $T_T (Pa \bullet s \bullet K^{-1})$
Q_2	Viscosity activation energy above $T_T (J \bullet mol^{-1})$
R	Gas constant 8.314 $(J \bullet mol^{-1} \bullet K^{-1})$
T	Temperature (K)
T_T	Phase transition temperature (K)
t	Time (s)
G	Grain diameter (m)
k_0	Grain growth pre-exponential factor $(\mu m^3 \bullet s^{-1})$
Q_G	Grain growth activation energy $(J \bullet mol^{-1})$
ρ_c	Grain growth critical density
C	Powder material fitting parameter
D	Powder material fitting parameter
I_1	First invariant of the stress tensor (Pa)
σ_x	X component of the stress tensor (Pa)
σ_y	Y component of the stress tensor (Pa)
σ_z	Z component of the stress tensor (Pa)
Z	Z spatial coordinate (m)
ρ_m	Mean relative density
ρ_a	Relative density amplitude
t_{layer}	Layer thickness (m)

sintering process, when full densification may be reached. For that, the initial characterization of any small or large heterogeneity is crucial for the BJT manufacturing industry.

Traditionally, the characterization of porous components has been carried out by means of traditional metallographic preparation methods: sample cross-sectioning, polishing, image acquisition and analysis. Due to the poor cohesion between the powder particles, high porosity in the green state and high brittleness of the green and especially brown (debinded) components, makes such an approach very time consuming, requires high level of manual expertise to be done appropriately and hence results in poor repeatability and reliability. Also, it limits the analysis to the cross-sectional 2D identification of the pores and particles, which makes it extremely difficult to properly characterize a heterogenous 3D porous structure. Recently, the use of X-Ray computed tomography (XCT) non-destructive techniques have been applied to the analysis of AM manufactured components [8–13]. For instance, proving to be very useful for the analysis of residual porosity of components produced by powder bed fusion – laser beam (PBF-LB) or electron beam (PBF-EB) when looking for large residual pores caused by lack of fusion, key-hole porosity, etc. [14]. The complexity of BJT components arises from their high porosity, which is defined by a complex internal pore structure with a wide distribution of pore sizes and shapes. This complexity continues to evolve from the green state throughout the sintering process [15]. Therefore, an extremely high-resolution technique is required for the accurate characterization of BJT components. In this work, the Synchrotron X-Ray computed tomography (SXCT) was used to characterize BJT samples and follow the ex-situ evolution of the pore/particle structure during the sintering process of stainless steel 316L BJT samples. Previous studies of other powder metallurgy (PM) components have shown the high definition achieved by this method [16,17], but a detailed characterization of the complete density range (green density to full density) has never been done for BJT components.

One of the key attributes of BJT parts is the arrangement of particles and the associated pore structure created by the layer-by-layer printing process. This structure is a critical initial condition for the sintering process, which could be tuned by the modification of the powder characteristics and printing parameters. For instance, the use of unimodal and bimodal powder size distributions has an impact on the evolution of the shrinkages and density during the sintering process [18]. Also, the tuning of printing parameters like layer thickness, binder saturation and powder recoating speeds influence the green density and the powder arrangement withing the green components [19]. Therefore, the understanding of this initial condition is crucial for the ability to predict the sintering behavior. Typically, a global average density is used to characterize and follow the evolution of the densification during the sintering process of PM components. This can be acceptable when the particles are arbitrarily and homogeneously distributed within the powder compact. However, due to the anisotropic nature of the BJT printing process used, variations of density and pore characteristics (e.g., size and shape) at the mesoscale level may occur [20,21]. Therefore, these heterogeneities must be considered when characterizing and predicting the BJT components' evolution during sintering. Typical heterogeneities from the layer-by-layer BJT printing (e.g., density and particle size) could be introduced in the macroscale modelling of sintering. In that case, the necessity of characterizing this initial condition can be solved by the high accuracy of the modern X-Ray based computed tomography techniques [8].

The evolution of initial heterogeneities during sintering is determined by an intricate combination of factors which include the applied sintering treatment, morphological characteristics of the pores (e.g., size and size distribution, shape), and the properties of the metal powder particles (size distribution, morphology, alloy composition, etc.). For instance, the sintering of multilayered composites has been previously studied and several modelling efforts has been done [22–25]. In this extreme case, the characteristic size of the internal heterogeneity (layer thickness) is relatively similar to the one of the components dimensions (total thickness), which leads to large bending distortions induced by different sintering kinetics. Other works have characterized the density and particle distribution heterogeneities within the BJT parts [21,26]. It has been shown that BJT printing may induce various levels of layer-by-layer density variation. Also, the particle size distribution strongly influences the amplitude of the density fluctuation along the building direction and its evolution during sintering. Finally, the sintering temperature is one of the major factors that determines the active sintering mechanisms and influences the density evolution with time. Density evolution, and hence final density and mechanical properties, are determined by combination of powder properties (powder theological properties, powder size and size distribution, powder morphology, alloy composition, surface chemistry, etc.) and printing process (layer thickness, printing parameters, hardware solution, etc.). Hence, change of the powder feedstock (even for the same material depending on supplier or powder batch) and/or printing or sintering parameters will

result in variation of the powder green density and its evolution during sintering. Therefore, a model that predicts the layer-by-layer characteristics variations, together with the macroscale evolution of the BJT samples microstructures, is required to understand impact of different parameters on initial green density and its evolution during sintering to assure robust BJT processing.

In the present paper, samples specially designed for SXCT were printed and sintered at different temperatures and times to follow the evolution of densification and porosity characteristics during the sintering cycle using Synchrotron X-Ray computed tomography (SXCT). Also, a continuum model of sintering previously developed for 316L BJT components [27,28] was used to predict the evolution of the density distribution along the building direction induced by the layer-by-layer BJT printing process. The simulation results were compared with the characteristic density distribution obtained from the SXCT characterization. Then, these results were used to discuss the implications of these inhomogeneities during the sintering of BJT components. The relationship between the internal stresses induced by differential shrinkage rates and the powder compact evolution were clarified based on the comparison between experimental characterization and modelling. Finally, other initial conditions of density and particle size distribution cases were implemented to reproduce potential cases of other particle size distribution and printing parameters.

2. Experimental methods

The samples used in this study were printed using the industrial DM P2500 binder jetting system (Digital Metal AB) with a layer thickness of 42 μm. Stainless steel DM 316L powder was used for the manufacturing, the chemical and physical properties of the powder are detailed in Table 1 and Table 2, respectively. Samples were debinded in air at 345 °C for 2 h. Then, several samples were pre-consolidated by pre-sintering in an industrial batch furnace under pure hydrogen atmosphere following 5 °C/min heating rate up to 900 °C with a dwell time of 1 h and final furnace cooling down to room temperature. The pre-sintering treatment was done to ensure safe handling of the component during the experiments due to the extremely small size of the specimens.

Synchrotron X-Ray computed tomography experiments typically require a small cylindrical sample to enable a high-resolution characterization of the internal porous structure. A cylindrical sample (0.7 mm in diameter and 5.5 mm length) with a rectangular base of 2 mm height (Z) and 5 mm sides lengths (X and Y) was designed, showed in Fig. 1. The samples were printed with the cylinder symmetry axis parallel to the building direction (Z axis). All the samples were printed using the standard printing parameters from Digital Metal BJT system developed for DM 316L powder used in this study.

2.1. Interrupted sintering experiments

The pre-sintered samples were sintered using a dilatometer Netzsch DIL 402C. The small tube furnace of the dilatometer is used to ensure high level of control over the sintering process in terms of temperature profile and processing atmosphere characteristics and hence assure sintering repeatability of the different sintering experiments performed. This is especially important due to the small size of the samples. The pushrod was blocked with an alumina spacer to leave free space at the end of the tube and avoid any contact with the sample during the sintering process, then the sample was placed on top of an alumina support. So, the dilatometer was used as a small precision furnace without any displacement being measured during the experiment. Typically, the 316L BJT sintering process require high temperatures up to 1370 °C to achieve high densification [21]. To characterize the microstructure evolution, interrupted sintering experiments were performed at 5 °C/min heating rate up to 1000, 1100, 1200, 1300 °C and 1370 °C with a dwell time of 2 min (for temperature stabilization purposes) followed by cooling at 30 °C/min down to room temperature. Also, an experiment at 1370 °C with a dwell time of 60 min was done to reproduce the complete sintering cycle for this material. Note that a different pre-sintered sample was used for each sintering cycle performed. The next sections will provide the details about the SXCT technique employed for the characterization (section 2.2) and the data post-processing methodology used (section 2.3).

Table 2
Physical properties of the 316L powder used.

Tap Density (g/cc)	D10 (μm)	D50 (μm)	D90 (μm)
5.0 (62.9 % rel. density)	8.0	16.0	26.0

2.2. Synchrotron x-ray computed tomography (SXCT)

The small cylindrical samples were characterized by computed tomography using synchrotron X-ray radiation (SXCT). The SXCT was conducted at the BAMline, BESSY II (Berlin, Germany), which is described in detail elsewhere [29,30]. The energy of the monochromatic X-ray beam was set to 45 keV with the voxel size of 0.7 μm. On-the-fly XCT was performed with 2400 projections acquired, each acquired with an exposure time of 0.5 s. On-the fly scans at the BAMline offer a drastic reduction of scan times while step scans offer flexibility in scanning schemes that are optimized to reduce ring artefacts or to offer a preview reconstruction already during the scan. The reconstruction of 3D volumes from 2D projections was made by BAM in-house developed software based on TomoPy [31].

A vertical section of around 1.5 mm in height from the pin was scanned using SXCT technique described previously (Fig. 1). After the 3D reconstruction, denoising and filtering, the data are available as grayscale stacked 2D slices. Then, each dataset file can be postprocessed (i.e., cropping and thresholding) to obtain the 3D binary data sets with two segmented phases (solid and porous) required for further comprehensive microstructural analysis.

2.3. SXCT data post-processing

The last step of post-processing is the analysis of the segmented (i.e., binary) microstructural data, which in this work can be divided into two main methods: analysis by 2D-slicing and the 3D analysis and rendering. The 2D-slicing analysis is used to reveal any microstructural preferential orientation related to the BJT printing process directions (e.g., building, recoating or binder deposition direction). In this process, the 3D data is sliced along different directions to obtain sequences of parallel 2D images that can be used to measure microstructural properties (e.g. relative density) as illustrated in Fig. 2. Two different slicing strategies have been designed and implemented using MATLAB 2021a image processing module:

- Slicing along the building direction (Z axis): a sequence of horizontal 2D slices perpendicular to the building direction were extracted for

Table 1
Chemistry of the powder used for BJT SXCT samples manufacturing.

Cr	Ni	Mo	Mn	Si	C	P	S	O	N	Fe
17.1	11.5	2.2	1.30	0.70	0.024	–	0.006	0.049	0.090	Balanced

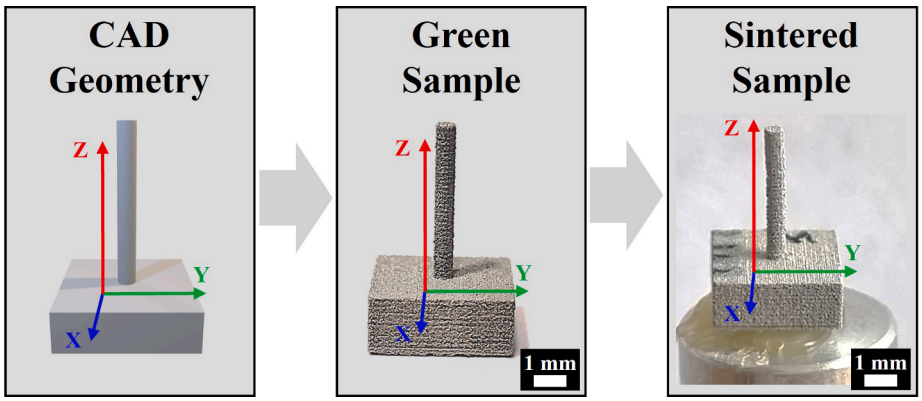

Fig. 1. Illustration of the designed CAD pin geometry, a BJT green sample and a sintered sample mounted on the SXCT stage. (For interpretation of the references to colour in this figure legend, the reader is referred to the web version of this article.)

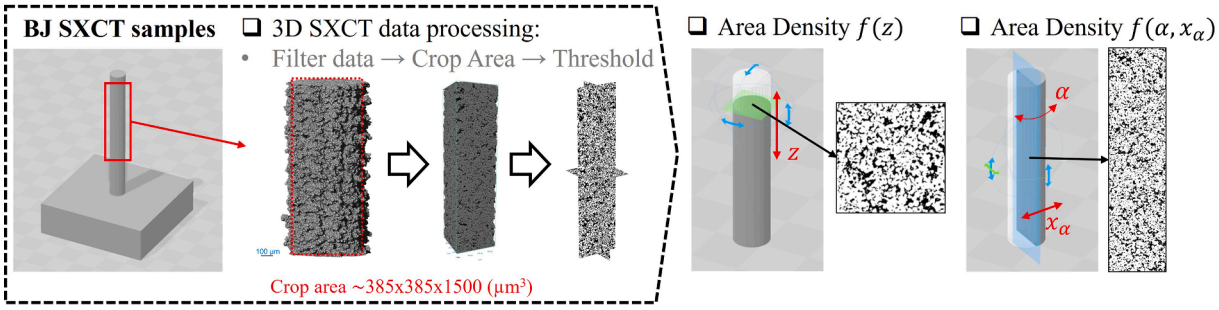

Fig. 2. SXCT data post-processing methodology.

each sample. The area density $\rho_z = f(z)$ was measured along the vertical direction.

- Slicing along different angled directions contained within the horizontal printing plane (XY plane): series of vertical planes were extracted for each sample, defined by the building direction and a perpendicular direction defined by an angle α. For each angle and orthogonal position x_α, the 2D slice was extracted and its plane area density $\rho_\alpha = f(x_\alpha)$ was measured. Note that the specific X and Y axis cannot be identified in the 3D data due to the cylindrical symmetry of the volume scanned.

Besides, other measurements can be done on the 2D microstructure slices. The particles were identified by segmenting the solid region using the watershed-based technique and their diameter was measured. Also, the pore surface area within each slice was calculated by multiplying the measured pore perimeter and the voxel size (0.7 μm).

In parallel, Dragonfly software [32] was used for further 3D analysis and rendering of 3D images. The open and closed porosity can be differentiated by separating the largest pore detected. The largest pore corresponds to the external space and the internal open porosity connected to it. However, this method is not suitable to characterize the interconnected porosity because it is connected to the external empty space of the dataset. Therefore, for samples with high interconnected porosity, the data should be cropped manually. This is the main reason for the internal cropping performed for the previous 2D-slicing quantitative analysis.

3. Results and discussion

As an initial qualitative analysis, the 3D dataset and the segmented internal porosity of each SXCT sample were rendered and shown in Fig. 3. The length of 1.5 mm of the scanned area is constant for all samples, but the shrinkage along the diameter of the sintered samples can be observed. The external surface topology shows the transition from individual particles of the green specimen (Fig. 3a) to the dense sintered structure of the fully sintered specimen (Fig. 3h). Also, Fig. 3 shows a section of the segmented porous structure from each SXCT sample's dataset studied (at the right side of each sample case). The rendered image consists of a partial bottom slice of the solid (gray) together with the segmented porosity colored by pore volume (μm^3). For the samples sintered al low temperature (Fig. 3 (a) to (f)), the major portion of the porosity consists of a single fully interconnected pore (red pore). In these figures, the largest pore was cut (385 μm x 385 μm) to account only for the internal porosity. The highly interconnected pore structure volume is being reduced and followed by the last stage of sintering represented by Fig. 3 (g) and (h), where closed pores can be identified in the region analyzed. Fig. 3 (g) shows the sintered structure at the end of the heating stage, where still large pores are present but not connected to the external surface. Finally, Fig. 3 (h) shows that after a 60 min holding at 1370 °C, the porosity consists of small isolated quasi-spherical pores, as was also shown previously [21]. In general, the average relative density increases with sintering temperature and time (a-h). However, a slight reduction of density was observed when comparing green (Fig. 3a), pre-sintered (Fig. 3b) and 1000 °C / 2 min sintered (Fig. 3c) samples. The expected densification of these samples is insignificant due to the low temperatures. Therefore, this slight difference might be attributed to different effects. The use of different samples subjected to ex-situ sintering may result in samples with slight density differences between 1 and 2 % due to small variations of density within the printing volume. Also, the green density measurement might be affected by the presence of binder on the sample, slightly increasing the actual relative density.

As detailed in section 2.2, the total volume and surface area were calculated for each sample's particle material and the closed porosity regions (after removing the largest pore connected with the external surface). During sintering, the total surface area decreases by 95.9 %

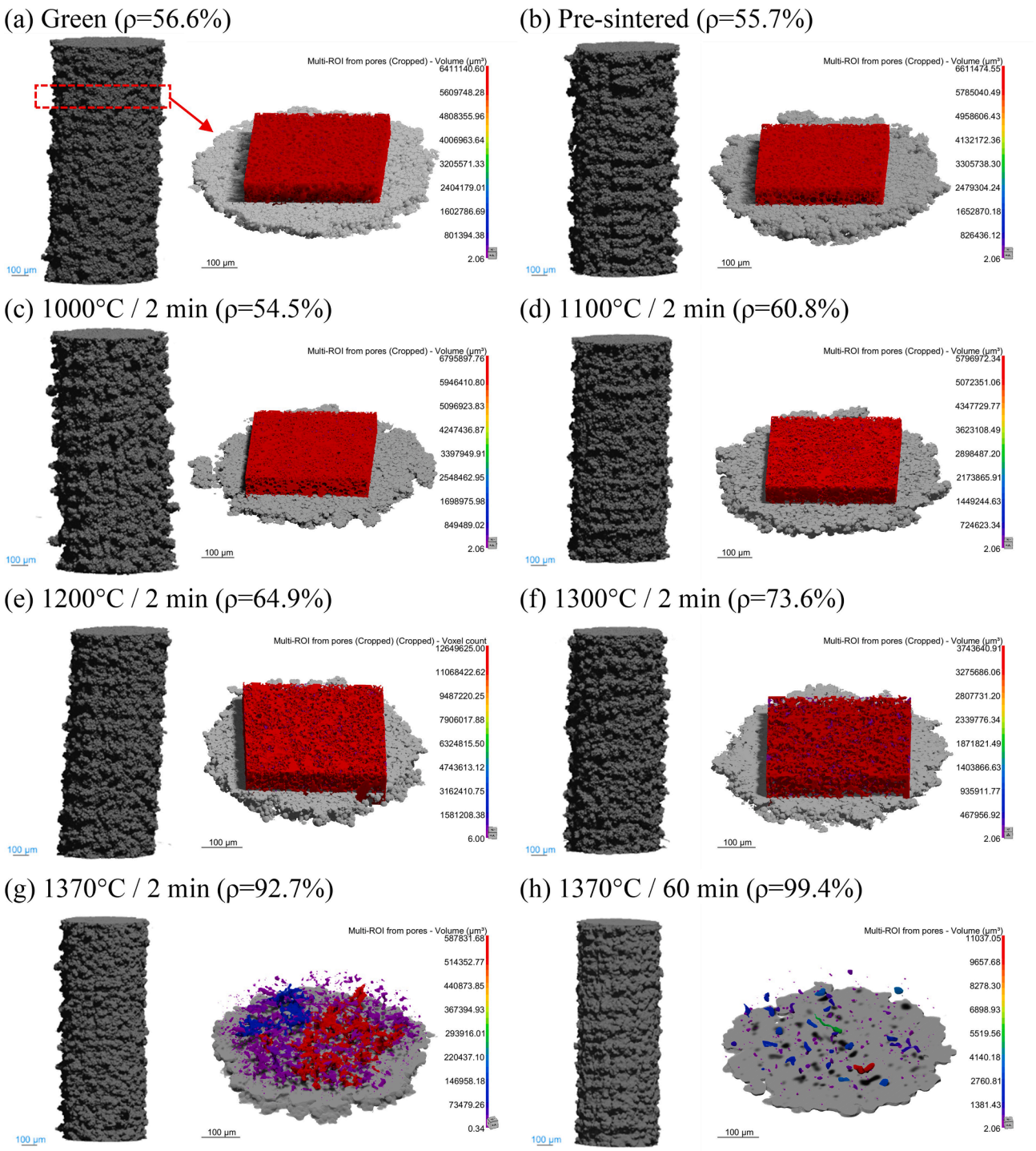

Fig. 3. 3D rendered image of the SXCT samples subjected to different interrupted sintering cycles. Also, a 3D slice of each sample is included on the right side, including the calculated pore volume.

(see Fig. 4a) while the measured material volume slightly increases by 12.6 % (from ~ 3.07E + 08 μm^3 to ~ 3.46E + 08 μm^3), particularly after sintering at temperatures > 1300 °C. This increase could be related to the challenging characterization of highly porous samples and the variability between samples used for ex-situ sintering dilatometry experiments. Also, during densification the surface area is reduced, and the accuracy of the material volume characterization improves. The closed porosity volume and surface area noticeably increase when densification process isolates pores by closure from the external surface (see Fig. 4b). In the BJT samples studied, this process is pronounced at temperatures above 1300 °C. This is most probably related to the enhanced diffusion and hence densification caused by the δ-ferrite transformation [20,21,33–35]. In Appendix A, the enhanced densification detected from the shrinkage behavior was discussed and the final microstructure of samples subjected to the full sintering cycle (1370 °C / 60 min) was shown, where the presence of residual δ-ferrite was observed. Finally, the closed pores shrink and produce further densification by reducing its surface area and volume.

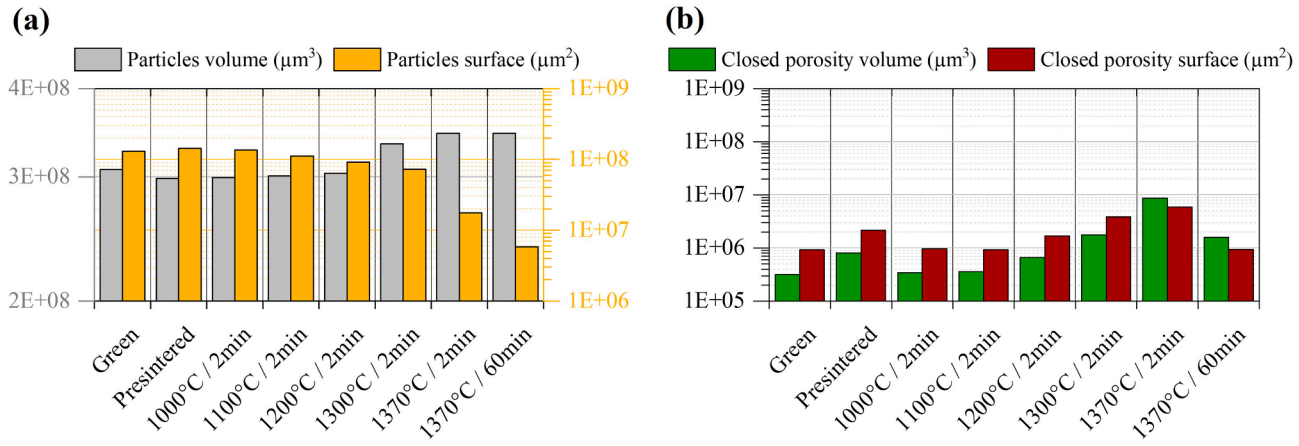

Fig. 4. (a) Measured particles (material skeleton) and (b) closed porosity volume and surface area for each sample dataset analyzed. Note that open porosity was excluded by eliminating the largest pore on each dataset.

3.1. Microstructure characterization along the building direction (Z axis)

One of the primary advantages of 3D CT characterization of porous materials is the possibility to perform density evaluation with high precision along any direction of the component. Fig. 5(a) shows the area density measured from parallel 2D slices oriented perpendicular to the building direction and with the smallest separation permitted by the 3D data voxel size of 0.7 µm (see section 2.3). The average density value increases with sintering temperature and time as shown in Fig. 5(b). The calculated standard deviation (SD) suggests that density fluctuation slightly increases during the heating stage of sintering, followed by a substantial decrease during the final sintering stage. Density fluctuations in BJT components have been characterized in previous studies [26], where a larger increase in the density fluctuation was observed for bimodal powder blends. In comparison, the increase in density fluctuation measured in the present study is negligible. However, the use of other BJT systems (i.e., printer) or powder particle characteristics (e.g., PSD, powder alloys) would affect the density fluctuation evolution [26]. Consequently, this can result in the emergence of undesirable heterogeneities or defects at both the macro- and micro-scale while undergoing sintering.

Fig. 5(a) exhibits a regular pattern of density variations,

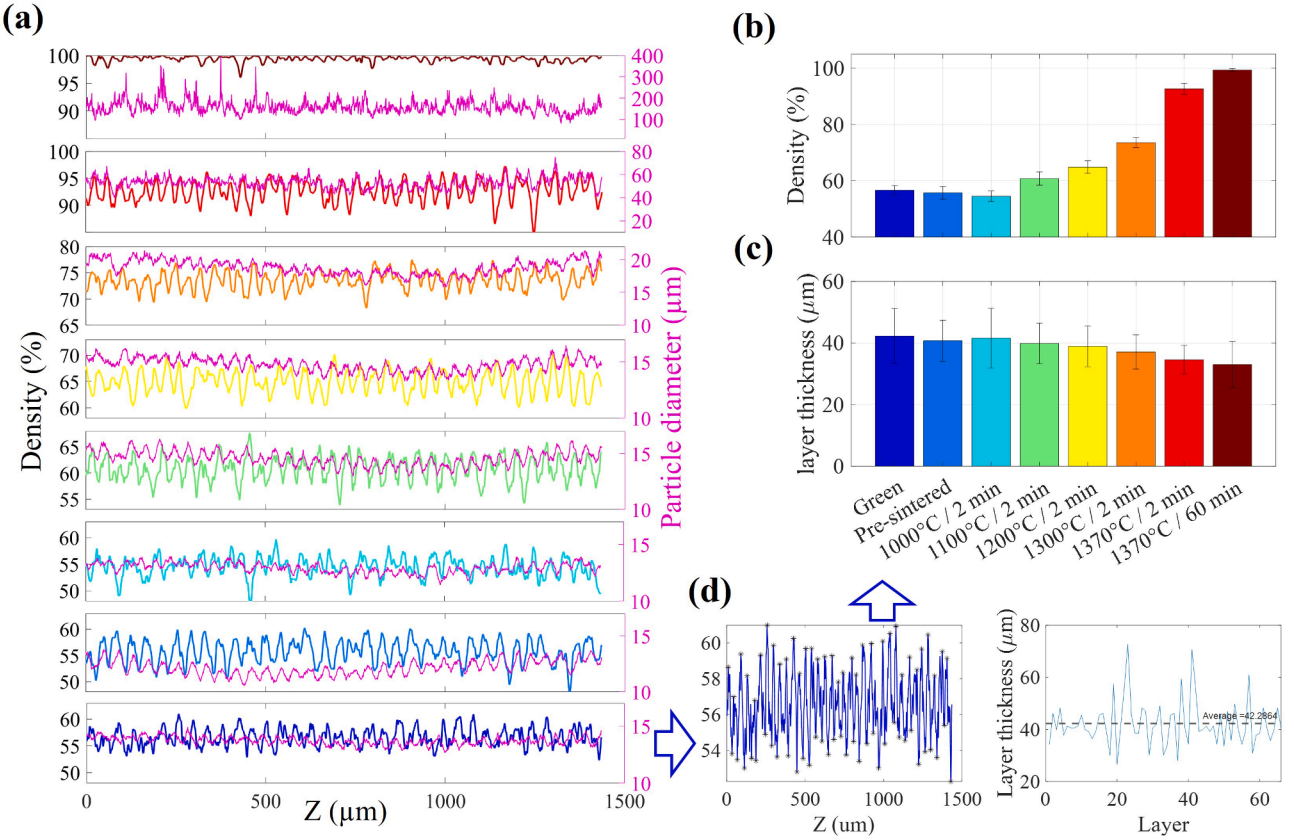

Fig. 5. Characterization of SXCT dataset for each sample along the building direction (Z) by 2D slicing method detailed in section 2.3: (a) density and particle size, (b) calculated average density and SD, (c) illustrative example of the peaks identification and layer thickness measurement, and (d) calculated layer thickness average and SD.

characterized by fluctuating densities between maximum and minimum peaks that appear uniformly spaced. During the analysis, minimum and maximum points were identified for each dataset (as illustrated in Fig. 5c). Then, the average and standard deviation (SD) of the distance between the maximum and minimum values, respectively, were calculated and results are plotted in Fig. 5(d). Surprisingly, the calculated value from the green and low-temperature sintered samples closely approximates to the BJT printing layer thickness of 42 μm. Consequently, the density periodicity of the porous structure identified in the 3D data can be directly related to the layer thickness used during the printing process. After full sintering, the distance between peaks decreases by ~ 21 % from ~ 42 μm to ~ 33 μm. This may suggest that the sample external dimensions and the internal layer spacing shrink equivalently during the densification process.

Fig. 6 (a) to (h) display 2D slice microstructure images that correspond to a pair of maximum and minimum density values for each sample, where details within the microstructure (i.e., particle/pore distribution) can be observed. In general, the evolution of interconnected porosity is evident as the temperature increases from the green sample (a) to the sample heated to 1300 °C (f). Then, further increase of sintering temperature at 1370 °C leads to a faster closure of the open porosity, as seen in Fig. 6 (g) and (h). This non-linear variation of the microstructure with the temperature is related to the enhanced densification rate caused by the δ-ferrite phase formed at high temperature ($\gtrsim 1300^{\circ}C$) [20,21,36,37], which can be observed on Fig. 5 (b). A comparison of the microstructures between the max and min points for each sample revealed homogeneous porosity distribution within the higher density slices, while the lower density slices showed some heterogeneity. Particularly, large pores were observed in the lower density slices, which were mostly densified after sintering at the highest temperature for 1 h as seen in Fig. 6 (h). Furthermore, the particle size obtained by the watershed segmentation reveals a similar periodic distribution of the particles size, where lower density regions show slightly lower mean particle size. However, no significant particle segregation can be observed between the lower and higher density slices in Fig. 6. Therefore, the particle size distribution detected can be related to the higher density areas having larger number of particles, which have particle sizes above the mean value. As discussed above, the low-ρ regions have larger pores which influences the number of particles within these regions.

3.2. Microstructure characterization along directions within the build plane (XY)

The stacking of powder layers is not the only recurring process that takes place during BJT printing. Also, the recoater-powder and binder-powder interactions systematically occur during each spreading and binder deposition step are taking in one specific orientation (powder spreading along Y-axis and binder deposition along X-axis), that can also lead to the inhomogeneity of the powder bed density and hence sintering anisotropy determined by the hardware solution. To recognize potential systematic microstructural heterogeneities related to the deposition steps of the printing process, the variation in density in 2D slices was measured using the methodology described in section 2.2 (see Fig. 2). The average density (solid line) and standard deviation (shaded area) for each angle α and sample characterized are shown in the left graph of Fig. 7. In general, the standard deviation values tend to increase with the temperature until 1300 °C, followed by a substantial reduction when sample reaches close to full density (1370 °C / 60 min). This can be related to presence of large pores until the delta-ferrite formation enhances diffusion and promotes the densification of these pores. Consequently, volume regions with smaller pores densified below 1300 °C and others remain with large pores, causing this increase on the scattering (standard deviation) of the density fluctuations. Besides, density variation along the angle with the largest standard deviation for each sample was extracted and plotted in the right side of Fig. 7. A profile with several maximum and minimum peaks from the density variation is present in most cases. However, as opposed to the density along the building direction, most of these profiles do not present the same consistency in the pattern observed.

Fig. 8 displays the microstructure (i.e., particle/pore distribution) from the 2D slices positioned at selected max and min peaks from each sample's density profile. A density difference from 3 % to 6 % was found between the max/min points evaluated. In Fig. 8 (a) to (d) it's difficult to observe a major difference in the microstructures, probably due to the highly interconnected porosity present in all these samples. Nevertheless, the microstructure at the min density peaks reveals some larger pore areas oriented along the horizontal direction. After higher densification was observed on samples from Fig. 8 (e) to (g), the larger horizontal pore areas were clearer and more consistent within the lower density slices. Then, this microstructural heterogeneity was eliminated by further isothermal sintering for 1 h at 1370 °C (see Fig. 8 (h)). These results may suggest that some "cratering" can be produced on top of the powder bed during the binder deposition process [9,10]. However, the X and Y directions of printing were not identified because of the cylindrical symmetrical shape of the samples, and the analysis along the envelope of angles α does not reveal a remarkable difference between any of the specific angles. Therefore, further focus of the discussion will be placed on the consistent heterogeneity pattern caused by the layer-by-layer printing process along the building direction discussed in the previous section.

In summary, the layer-by-layer BJT printing process induces a consistent density fluctuation pattern caused by areas of larger porosity along the building direction (see Fig. 9). The periodicity of this density variation consistently decreases during the densification process which is directly related to the sample's shrinkage. The initial period is equal to the BJT printing layer thickness of 42 μm and decreases down to ~ 33 μm. In addition, the microstructures in Fig. 6 reveal that the pore structure heterogeneity is present until the last stage of the sintering process. A possible explanation is that the intralayer areas densify faster, while the interlayer areas with larger porosity densify later at the end of sintering, when the enhanced densification is enabled by improved material transfer and e.g. the δ-ferrite phase transformation. Furthermore, SD of density along the building direction (Z) varies during the sintering process. In the present study, a slight increase on the SD was followed by a rapid decrease at the final sintering stage. However, this behavior likely depends on the powder particle size distribution and sintering conditions (e.g. time and temperature) [26]. For instance, bimodal particle size distribution can lead to high segregation within the microstructure and strong increase in the density amplitude when sintering at low temperatures so that low global densification is achieved. Another effect revealed by the SXCT characterization is the "cratering" effect potentially caused by the binder-powder and/or recoater-powder interaction during the printing process. This effect is not as pronounced and consistent, which suggests the reliable performance of the BJT manufacturing system, and the process used during this study.

The formation of these pore characteristics within the BJT green components is directly related to the different BJT printing steps that come into play. An illustrative diagram is shown in Fig. 9, which exposes the different mechanisms and their potential effect on the powder particles arrangement. First, the powder deposition and recoating are completed to achieve a uniform layer with the required thickness. This part of the process shapes a characteristic particle/pore distribution within the layer, governed by the type of recoating system (e.g., wiper, counter- or forward-rotating roller), the printing parameters (e.g., roller transverse/ rotating speed) and the particle characteristics (e.g., particle size distribution). Also, during the binder deposition, the kinetics of the binder impact on the particles may modify the particle/pore distribution (e.g., cratering on the top surface). Then, the next layer of powder is spread and recoated on top of the previous layer. However, the bottom powder movement is now restricted by the binder, thus affecting the powder flow within the interlayer region. This might reduce the global

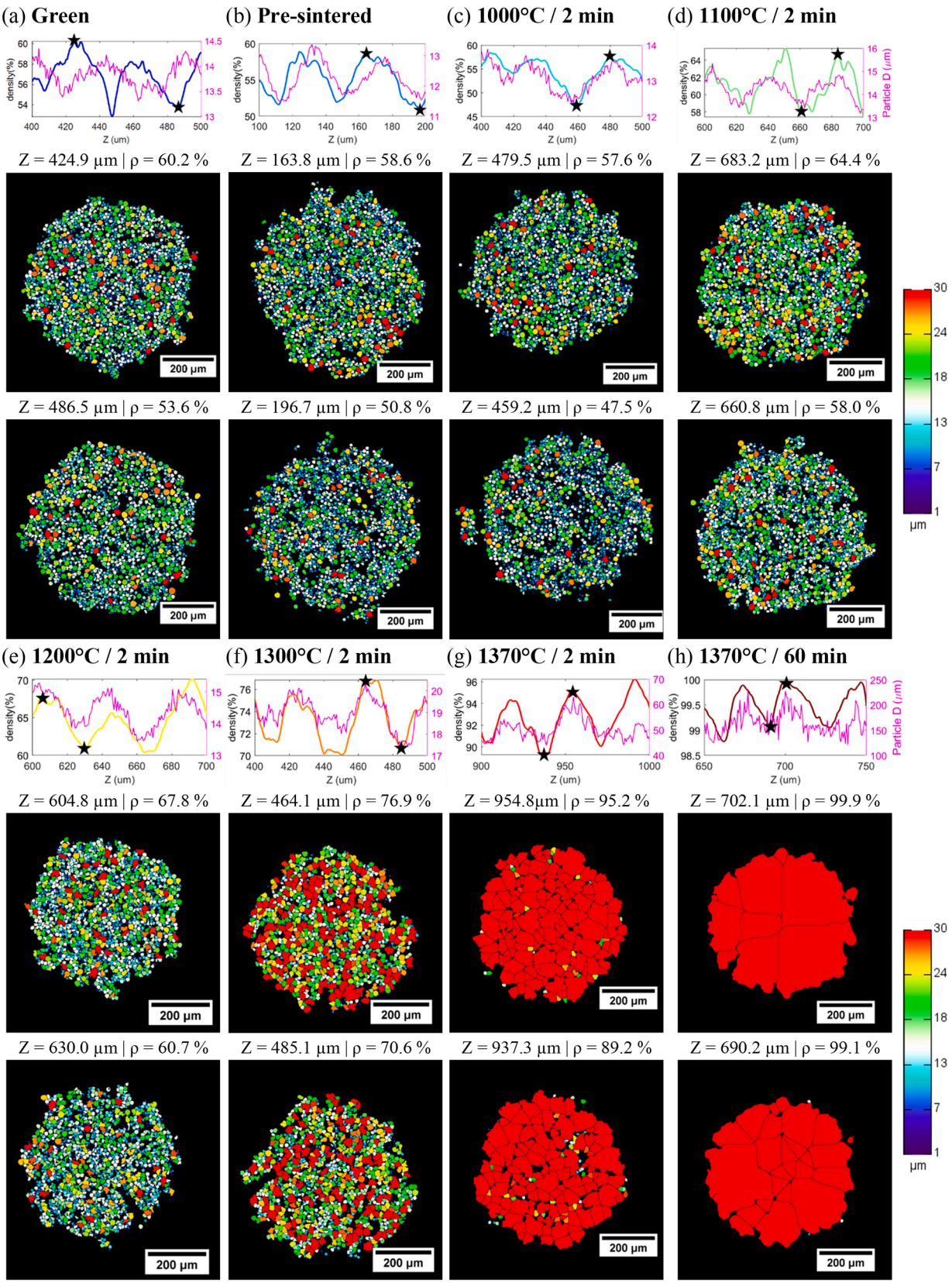

Fig. 6. Detailed Synchrotron X-Ray CT microstructure data analysis of each sample: from green (a) and pre-sintered (b) samples to samples subjected to different interrupted sintering from 1000 °C to 2 min (c) to 1370 °C-60 min (h). For each sample (a-h) a certain region of the density and particle diameter fluctuation along Z was plotted (top graph), where points of high and low density were indicated by a star icon. Below this graph, the cross-sections images extracted from the 3D SXCT data are shown, where the particles from watershed segmentation are colored as function of the diameter. (For interpretation of the references to colour in this figure legend, the reader is referred to the web version of this article.)

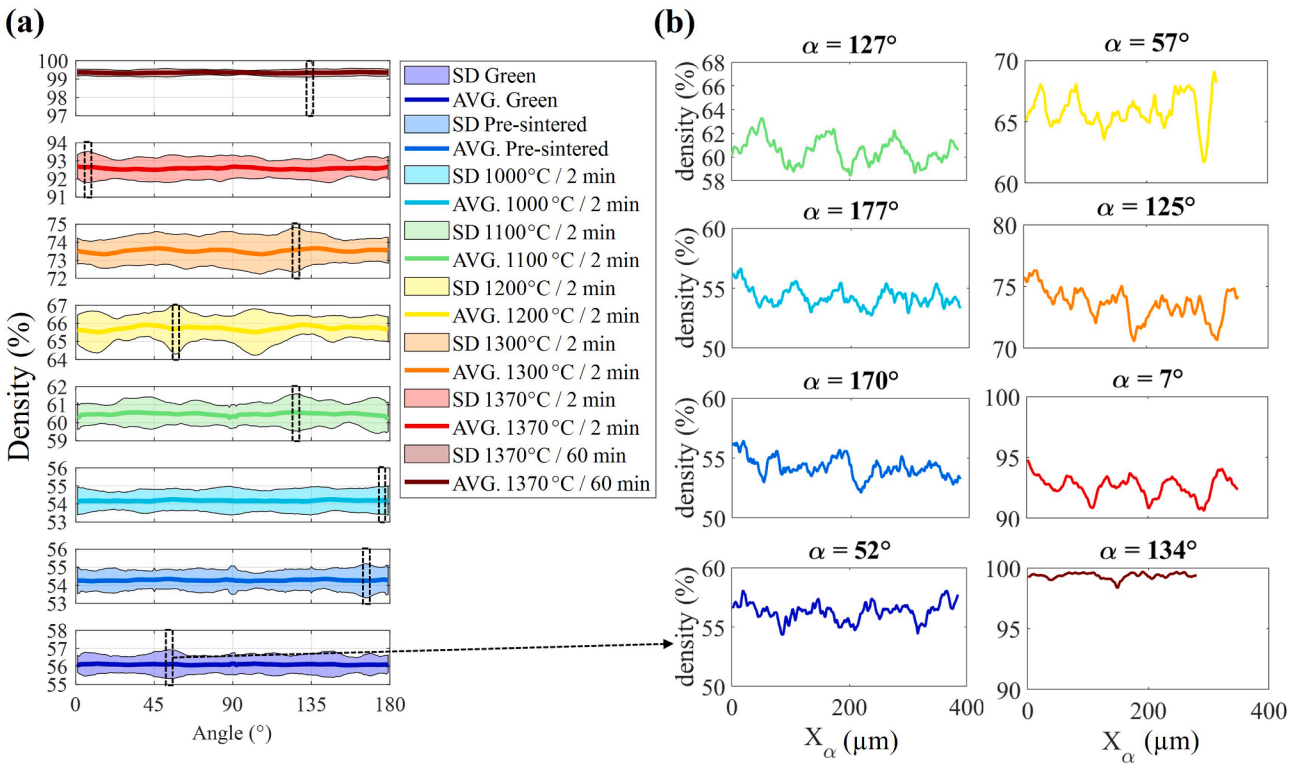

Fig. 7. Measurement of 2D area density from each sample dataset along each X_α axis, according to methodology in section 2.3. (a) Averaged density and SD of density profile measured along X_α (from $\alpha = 0°$ to 180°) for each sample. (b) Density profiles along the indicated angles, which have the highest SD value.

green density of the BJT printed components and induces the density variation along the building direction [38]. Furthermore, when wide or bimodal particle size distributions are used, various printing conditions may induce strong particle segregation during printing. Previous studies have revealed this effect by using computer models [39,40] and experimentally [26]. Again, the level of segregation depends on the same factors, being more severe for spreading systems based on rollers [39].

From this schematic description, the complex relationship between the printing process and the porous green structure of the BJT components can be observed. The characterization and modelling of this green structure is highly relevant for the development and implementation of the modelling of sintering, required for improved process understanding and increasing process robustness. Previous research attempted to understand the connection between the powder printing process (discrete element method) and the sintering process simulation [41]. However, significant simplification was done by the assumption of homogeneous distribution of the green density and particle size used as initial conditions for the sintering model. Therefore, to unlock the full potential of this approach, the specific density and particle size distribution can be included in the sintering model. A way to include these factors in a sintering simulation for BJT components will be further discussed in section 4.

3.3. Estimation of sintering stress from the SXCT characterization

The driving force during the free sintering is related to the internal pore surface area evolution. Therefore, SXCT data can be used to calculate this driving force from the evolution of the characterized 3D pore structure during sintering [12,42,43]. Fig. 10(a) shows the total pore surface area measured from each sample. Also, the surface area was measured for each slice (1 voxel = 0.7 μm thickness) along the building direction (Z axis). In Fig. 10(b), the pore surface area is plotted against the relative density of each slice. Note that the cropped datasets were used to eliminate the external surface which does not contribute to the sintering driving force. Minor reduction of pore surface area occurs during the early stages of sintering (up to 1300 °C), while density slightly increases by ~ 10 %. This can be related to a combination of minor particles rearrangement followed by neck formation and slight neck growth, which does not highly contribute to pore surface reduction [44]. The distribution of pore surface area along the vertical direction reveals the different kinetics of the sintering within diverse regions of the layered porosity. Low-density regions have less pore surface area compared to the high-density regions. After the interrupted sintering at 1300 °C and beyond, it appears that this trend is reversed during the sintering process.

The sintering stress can be defined as the derivative of the free energy per unit mass with respect to the volumetric mass of the porous material [45]:

$$P_L = \frac{dF}{dV} = \frac{dF}{dS} \bullet \frac{dS}{dV} \tag{1}$$

where F is the free surface energy, V is the pore volume and S is the pore surface area. The first term is a material constant defined as the surface tension $dF/dS = \alpha$. Therefore, the sintering stress can be expressed as:

$$P_L = \alpha \frac{dS}{dV} \tag{2}$$

Accordingly, the variation of the porous surface area and volume measured from the SXCT data can be used to calculate the sintering stress evolution of the BJT 316L samples. The previous analysis confirmed the existence of a fluctuating porous structure, which can be divided into low-density and high-density regions. Following this idea, the sintering stress was calculated within the two different regions by separating the data below and above the average density value (see Fig. 11). The continuous evolution of the pore volume and surface area can be well described by a third-degree polynomial approximation, which was fitted to the SXCT experimental data. Then, a normalized sintering stress P_L/α plotted in Fig. 11 was obtained using eq.(2). The

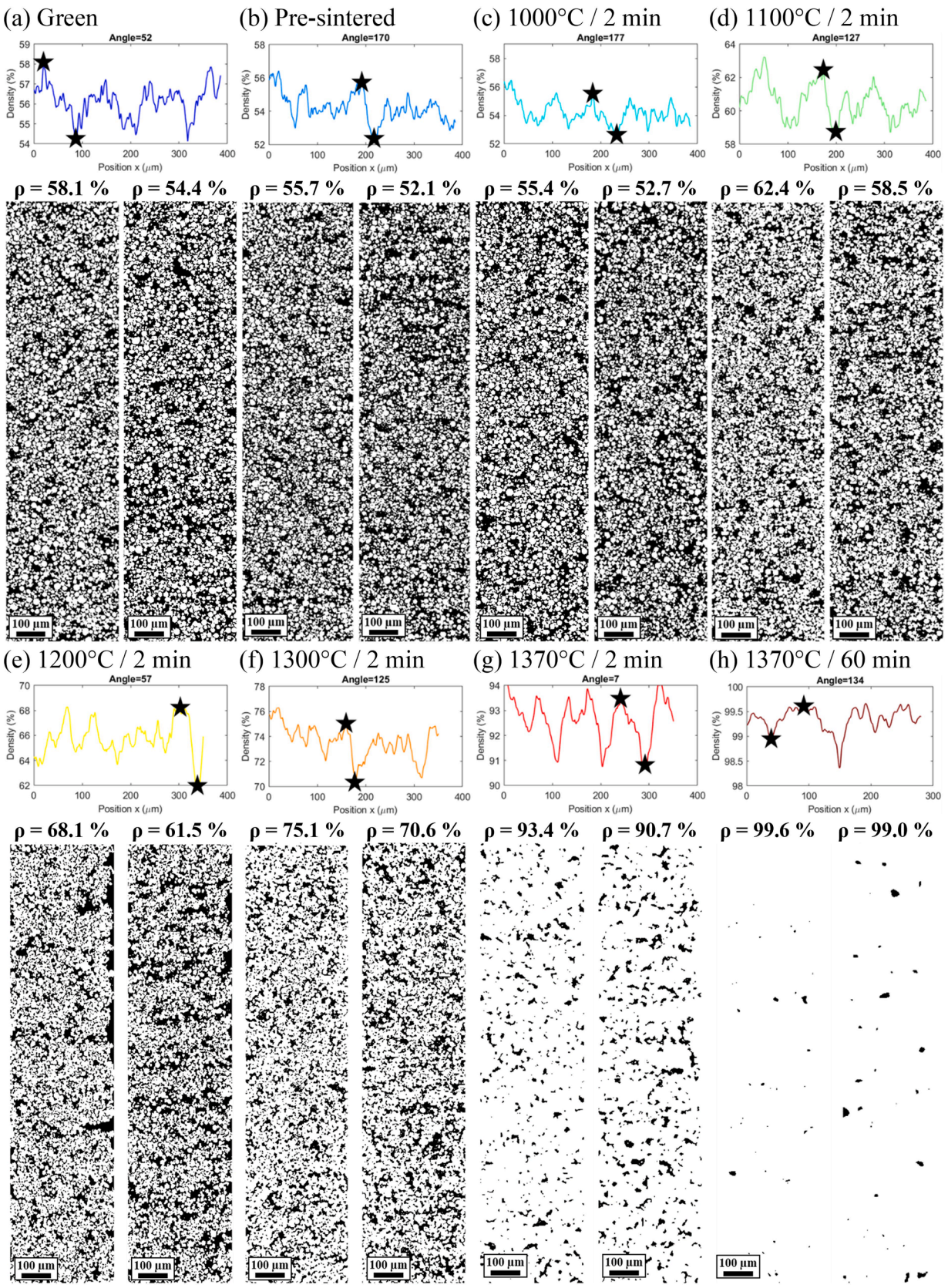

Fig. 8. Vertical cross-section images of each sample (a-h) segmented SXCT data extracted from a maximum and minimum density point. A graph with a zoom section of the density profile was shown to indicate the X_α position of the cross-sections shown below of each density fluctuation graph (star scattered points indicate the position of the cross-sections).

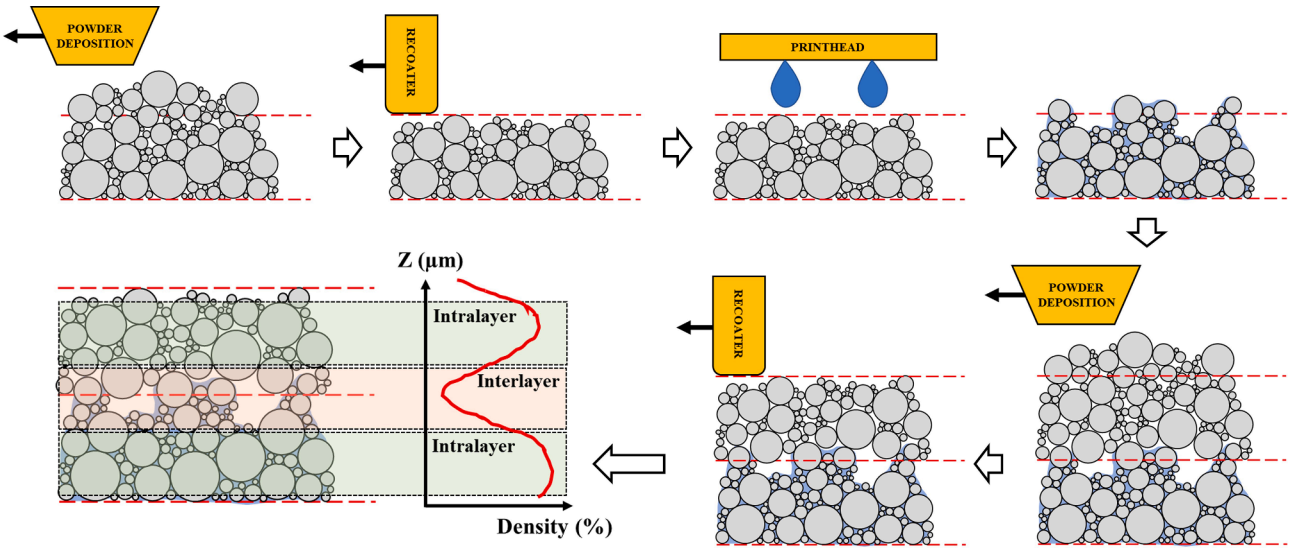

Fig. 9. Schematic illustration of the powder particles arrangement during the different steps of the BJT printing process. Also, an estimation of the attained green density distribution along the building direction is shown. (For interpretation of the references to colour in this figure legend, the reader is referred to the web version of this article.)

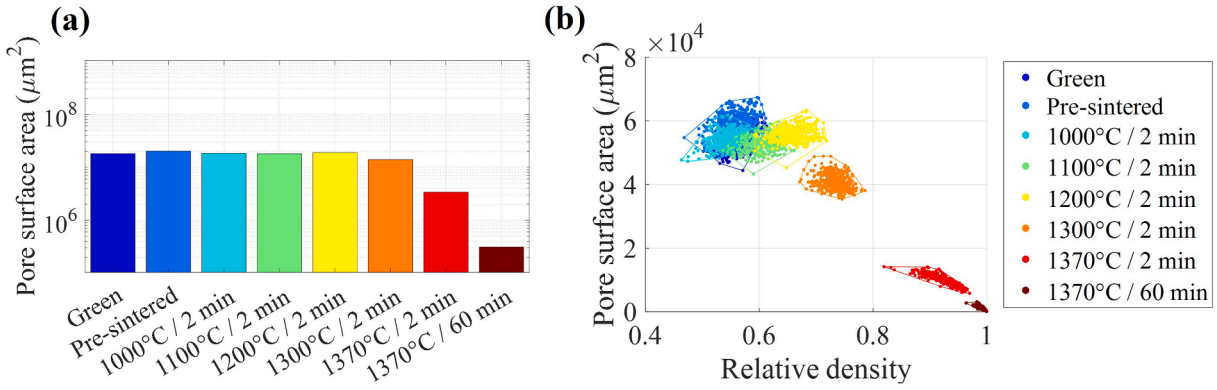

Fig. 10. Measured pore surface area of cropped SXCT for each sample dataset: (a) total pore surface area, (b) pore surface area plotted against the relative density for each XY slice.

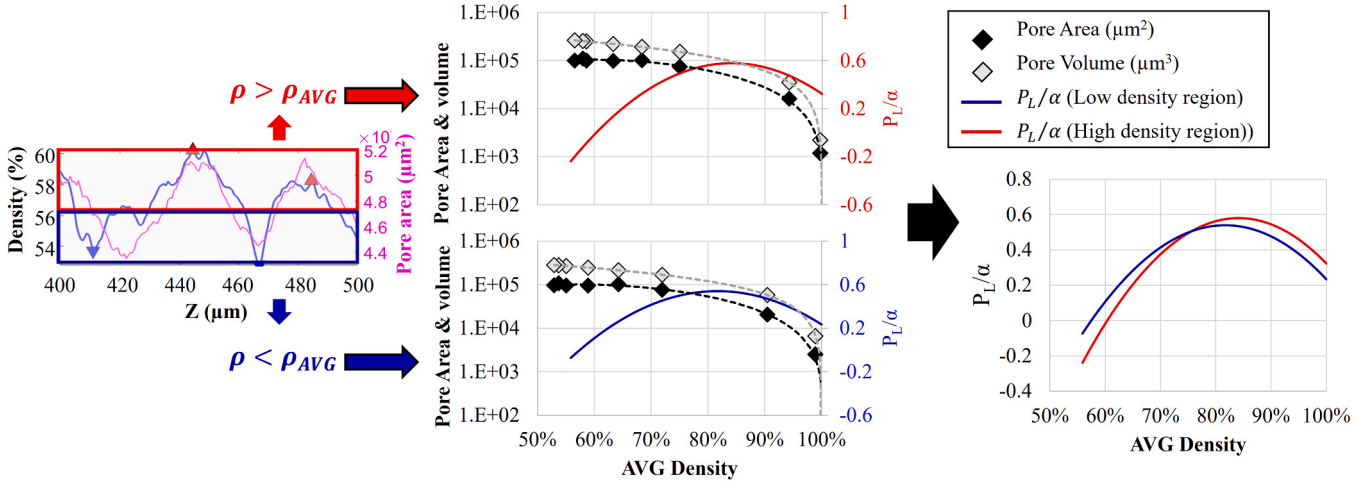

Fig. 11. Sintering stress calculation from the pore volume and surface area measurements of SXCT samples.

evolution of sintering stress during the sintering process was slightly different for each region, in accordance with the previously discussed pore surface evolution. Initially the sintering stress is higher in the low-density regions, but during the intermediate sintering this behavior switches in favor to a higher sintering stress on the high-density region until the end of sintering. However, both calculated values are relatively close. In general, the sintering stress increases until a relative density of ~ 85 % and then decreases. The grain diameter is typically used to estimate the sintering stress kinetics using equation (3) [46,47]. This is based on the connection between the grain and pore radius evolution during sintering. Later this equation will be used within the constitutive relationship used for the modelling of sintering.

$$P_L = 3\alpha\frac{(1-\theta)^2}{G/2} \tag{3}$$

where α is the specific surface energy, θ is the relative porosity and G is the grain size.

4. Model and simulations

A model of sintering for 316L components manufactured by BJT, based on the continuum theory of sintering [45], has been developed in previous studies [27,28]. The specifics of the BJT porous structure were included in the formulation of the material constitutive behavior, and the corresponding material constants were previously calculated [27,28]. Also, the effect of δ-ferrite transformation on the sintering behavior of 316L BJ components was studied and included in the solid material viscosity [28]. Originally, these studies have been performed assuming homogeneous initial conditions using the averaged green density and particle/grain size within the components. However, the FEM implementation of the continuum mechanic sintering model allows for introduction of fluctuating initial values for the state variables (i.e., density). Therefore, in this study the effect of introducing and varying the characterized layered BJT structure in the simulation initial conditions will be evaluated.

4.1. Sintering model of 316L BJT components

The model used considers the linear-viscous case for free-sintering process applied to components manufactured using BJT. Therefore, the general material constitutive equation used can be formulated as follows:

$$\boldsymbol{\sigma}_{ij} = 2\eta_0\left[\varphi\dot{\boldsymbol{e}}_{ij} + \left(\psi - \frac{1}{3}\varphi\right)\dot{e}\delta_{ij}\right] + P_L\delta_{ij} \tag{4}$$

where η_0 is the shear viscosity of the porous body's skeleton material (i.e., shear viscosity of the fully dense body), P_L is the effective sintering stress and δ_{ij} is the Kronecker delta function. φ and ψ are functions of porosity that characterize the normalized shear and bulk moduli of the porous compact, and $\dot{e}$ is the volumetric shrinkage rate.

The normalized bulk viscosity (5) and normalized shear viscosity (6) equations were previously developed for the material used [27]:

$$\psi(\theta) = \frac{2}{3}\frac{(1-\theta)^C}{\theta^D} \tag{5}$$

$$\varphi(\theta) = (1-\theta)^2 \tag{6}$$

Then, the grain growth kinetics follows the following equation [48]:

$$\frac{dG}{dt} = \frac{k_0}{3G^2}\left(\frac{1-\rho_c}{2-\rho_c-\rho}\right)^{3/2} exp\left(\frac{-Q_G}{RT}\right) \tag{7}$$

The model presented above was expanded to include the high-temperature stage of sintering of BJT 316L, which includes the effect of the δ-ferrite transformation on the solid material viscosity [28]:

$$\eta_0 = A_i T exp\left(\frac{Q_i}{RT}\right)\begin{cases} i = 1 \rightarrow A_1 Q_1\,, & \text{if } T < T_T \\ i = 2 \rightarrow A_2 Q_2\,, & \text{if } T \geq T_T \end{cases}$$
$$\text{where : } T_T = \frac{Q_2 - Q_1}{R ln\left(\frac{A_1}{A_2}\right)} \tag{8}$$

All the material constants used in the simulations (see Table 3) were obtained by using experimental dilatometry and microstructural data from [27,28].

Finally, the sintering model proposed was solved using the finite element method (FEM) by its implementation in the FEA software COMSOL Multiphysics 6.0.

4.2. Modelling results and discussion

The sintering model described in the previous section was used to simulate the sintering process of BJT samples, introducing the internal microstructural variation obtained from the SXCT experiments. In the first case, the SXCT sintering experiments were virtually reproduced by introducing the green density along the building direction $\rho_z = f(z)$ as initial condition. Later, a detailed analysis was performed by simulating an ideal representative volume element (RVE) of the periodic structure. The temperature field was imposed as a function of the sintering time to reproduce the full experimental sintering test: heating at 5 °C/min up to 1370 °C with a dwell time of 60 min, followed by cooling at 30 °C/min down to room temperature. It is assumed that the sintering is negligible during the 2 min holding and cooling steps of the interrupted dilatometry sintering tests. Thus, direct correlation can be done between the simulation of the full sintering test at the corresponding simulation times against the interrupted sintering experimental data.

4.3. SXCT sample virtual sintering experiment

The sintering of the pin characterized by SCXT was reproduced by the simulation using the model presented above, where the green density ρ_z (see Fig. 5) was used as the initial condition. First, the initial and final 3D geometry is plotted in Fig. 12(a), where the volume shrinkage can be observed. In general, the density increases and fluctuation evolution during sintering is well replicated by the model, as seen in Fig. 12 (b). However, slightly larger densification is obtained by the SXCT experiment, which could be related to the extremely small size of the pin. Note that the model was fitted by experimental data from larger samples (10 mm cubes) which final measured density was ~ 97 %. The standard deviation (SD) of the density values is used as a measurement of its fluctuation along Z. The density average and SD is compared between the model and the SXCT data in Fig. 12(c). The SD evolution reveals a slight increase in the density fluctuation, followed by a rapid decrease down to SD ~ 0.5 % at the end of the sintering.

The increase of the density fluctuation of BJT samples has been previously reported in other studies [26]. There, samples sintered at low densification temperatures showed an increase in the density fluctuation, and samples sintered at high densification temperatures showed a decreased density fluctuation. Moreover, the effect of the particle size distribution was revealed. Particularly, samples printed with bimodal particle size distribution showed a remarkably increase in the density fluctuation range (Δ~16.7 %) after sintering at low densification temperatures (Δρ < 3 %). However, the monomodal powder blends showed a much smaller increase in the density fluctuation range. Similarly, the powder used in this study showed minor increased density fluctuation at low densification temperatures followed by a large decrease when densification rate increases. The effect described can be related to the concept of sintering instability that may arise during the sintering of heterogenous powder compacts due to internal variation in shrinkage

Table 3
Material constants for the sintering continuum model simulations of the 316L BJT samples [27].

C	D	A_1/α [s/K m]	A_2/α [s/K m]	Q_1 [KJ/mol]	Q_2 [KJ/mol]	k_0 [$\mu m^3/s$]	Q_G [KJ/mol]	ρ_c
11.35	0.49	8.993	5.33e-32	201.7	1178.7	29.65e-5	164.8	0.9486

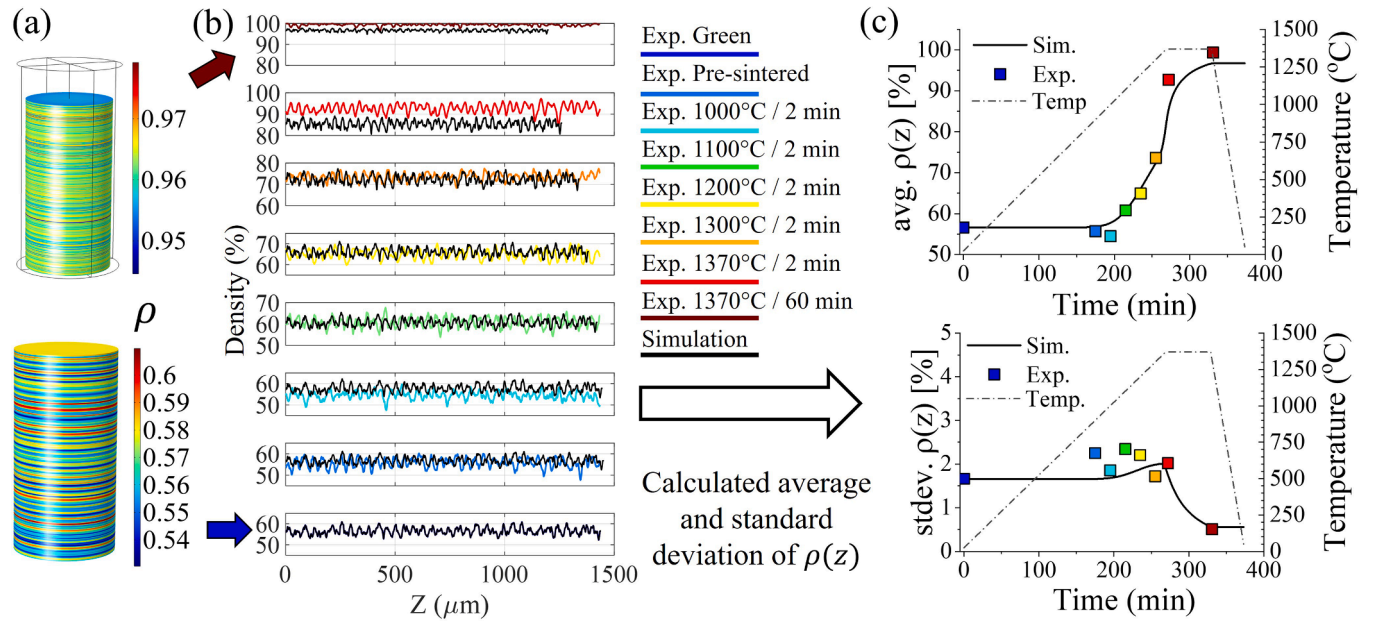

Fig. 12. Evolution of SXCT sample during sintering: (a) 3D volume plot at the beginning and end of simulation, (b) comparison between model (black line) and experiments density fluctuation along the building direction, (c) calculated density average and standard deviation for each sample (SXCT experiment vs model results).

kinetics [49–51]. In extreme cases, these instabilities may even lead to cracking or defects growth during sintering. However, this temporal instability faded later during the sintering process of BJT components at higher temperatures, transitioning into a more homogeneous internal sintered structure. In the next section, a detailed RVE simulation will be useful to elucidate about the different contributions that generate this effect during the sintering process.

4.4. Representative volume element simulation of the periodic BJT structure

The observed BJT density periodic structure along the building direction was approximated using a sinusoidal periodic function with the same average, SD and periodicity of 42 μm. Then, the smallest part of the periodic structure was reproduced, and the sinusoidal function implemented with values to match the experimental green density fluctuation as detailed in Fig. 5. The low- and high-porosity regions corresponds to the interlayer and intralayer regions of the BJT structure, respectively (see Fig. 11). It is known that non-symmetric porous laminates experience bending deformation during sintering [22,23,25,52]. Therefore, a symmetrical structure (i.e. low–high-low density) as illustrated in Fig. 13(a) was implemented to avoid bending deformation and focus the analysis on the evolution of the density fluctuation.

During pressure-less sintering, the external stress contribution in eq. (4) is equal to zero. However, in heterogeneous materials, internal stresses may arise and contribute to constraining or accelerating the sintering process within different regions of the component. Here, the hydrostatic strain rate is the main contribution to the densification of the continuum model presented which can be formulated as follow:

$$(\dot{\boldsymbol{\epsilon}}_{ij})_{hyd} = \frac{I_1 - P_L}{K}\delta_{ij} = \frac{(\sigma_x + \sigma_y + \sigma_z)/3 - P_L}{6\eta_0\psi}\delta_{ij} \quad (9)$$

A more comprehensive analysis of the heterogenous porosity on the sintering model can be obtained by analyzing the evolution of each stress term at different regions of the part. Fig. 13(b-d) show the evaluation of the averaged value of the stress terms in eq.(9) calculated within the low-ρ, high-ρ and the complete volume. The evolution of the first stress invariant (I_1) revealed the low-ρ regions (interlayer) in tension state, while the high-ρ regions (intralayer) are in compression. This differential stress gradually decreases towards zero during sintering because of the internal structure homogenization. Specifically, these stresses mostly occur along the X and Y directions (see Fig. 13b) because of the constrained differential shrinkage rates between the different layer sections (low-ρ and high-ρ). However, in the vertical direction the strains within different layers are less constrained by other layer regions (due to the vertical stacking of the layers), thus negligible internal stresses occur along this direction. This reveals a transverse isotropic behavior caused by the layer-by-layer density fluctuation. In Fig. 13(c), the sintering stress kinetics shows similar behavior to the experimental measurements, with a maximum sintering stress occurring at ~ 85 % density (see Fig. 11). In conclusion, despite the discussed local tension contribution, the sum of hydrostatic and sintering stresses results on a distribution of compressive stresses within the whole simulated volume. This ends in continuous densification driven by the simultaneous reduction of the effective bulk viscosity K, without any local swelling.

The case studied from the experimental SXCT data showed a stable sintering densification, which leads to a final homogenization of density. However, other extreme cases can occur when bimodal powder blends are used and/or the printing process is not optimized, thus large pores and heterogeneities are present in the green component [26,40,41]. To illustrate such case, the effect of a severe particle segregation during BJT printing of bimodal powder (1 μm to 130 μm) is implemented via the grain size distribution along the building direction $G(z)$ (see Fig. 14a). Also, the layer thickness was changed accordingly and set at 150 μm

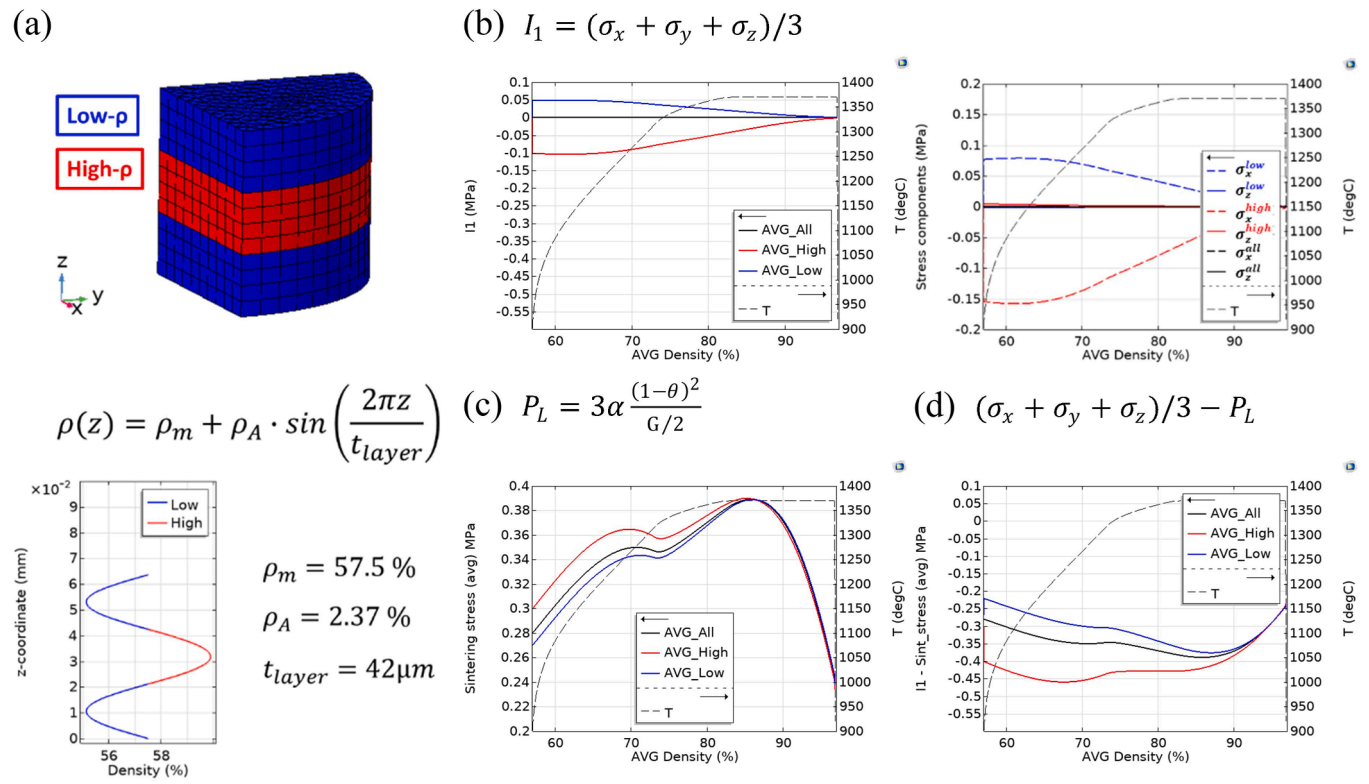

Fig. 13. RVE simulation results of the sinusoidal density fluctuation: (a) identification of the low-ρ and high-ρ regions and sinusoidal function of density fluctuation, (b) First invariant of stress and stress components calculated from simulation results, (c) sintering stress from the different regions, (d) sum of internal stresses and sintering stress.

with a density fluctuation between 49 % and 61 %. Typically, the relative distribution of density is related to the particle arrangement during printing, which may be measured or simulated by other modelling approaches like discrete element modelling (DEM) [38,40,41]. In this study, three different cases were addressed, where the relative position between the initial density and particle size

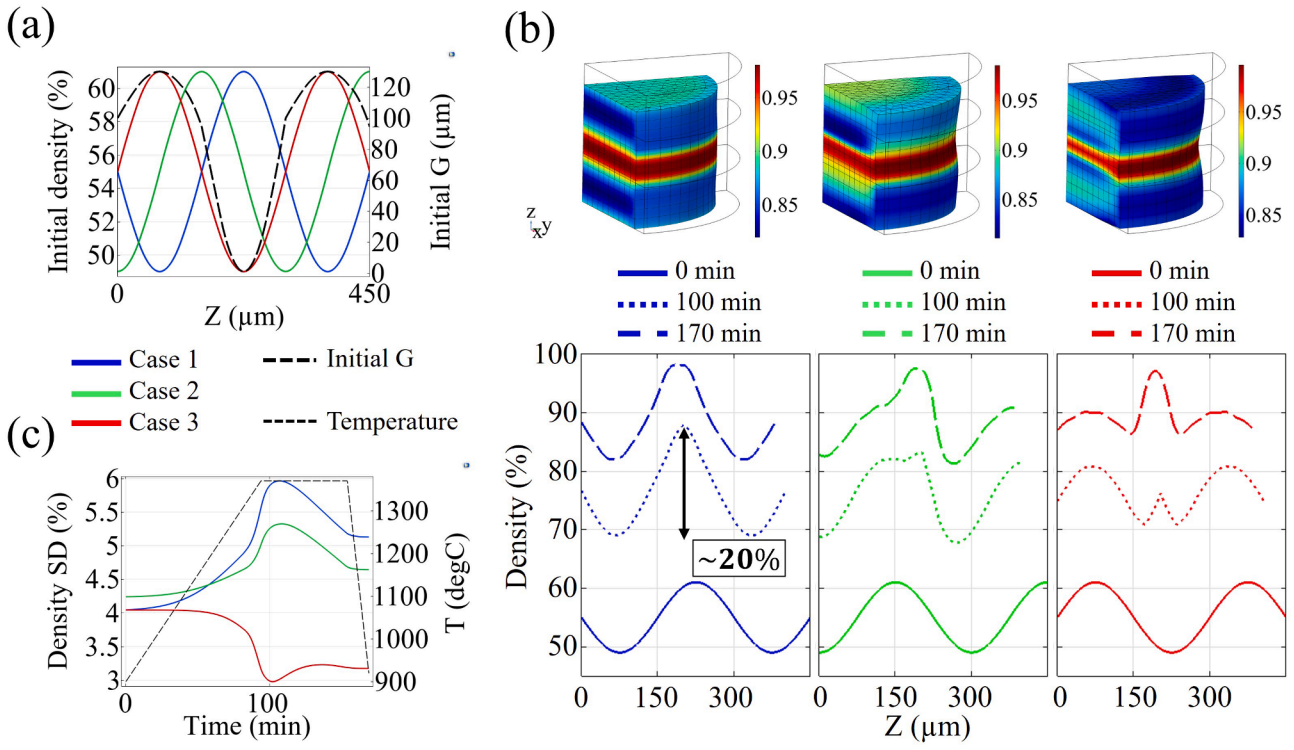

Fig. 14. Sintering simulation results for each density and-particle size distribution cases (1, 2 and 3): (a) initial conditions of G(z) and ρ(z) for each case, (b) results of density fluctuation ρ(z) at different times during sintering, (c) calculated standard deviation of the density fluctuation for each case during the sintering simulation.

distribution were varied as shown in Fig. 14(a).

The same sintering cycle used for the SXCT experiments was simulated. Fig. 14(b) shows the final 3D density distribution and the evolution of the density profile. In the first case, the high-ρ match the position with the low grain size region (low-G), which leads to larger sintering stress in this region. The result is a remarkable increase of ~ 10 % on the density fluctuation during the intermediate sintering, followed by a minor decrease during the isothermal step. This behavior was illustrated by measuring the SD of the density profile, plotted in Fig. 14(c). This model outcome is a good example of the potential sintering behavior of extremely wide powder size distribution, which can be observed in other experimental studies of BJT sintering [26]. Note that to replicate the results the model parameters should be adjusted to the powder material used in the experiments, which usually requires extensive characterization [27]. The second and third cases are a modification of the relative position between $G(z)$ and $\rho(z)$ by shifting $\rho(z)$ 75 μm (case 2) and 150 μm (case 3). In the second case, the density fluctuation has a similar behavior but with a lower increase during the intermediate sintering and a shape modification of $\rho(z)$. Lastly, in the third case the low-G and low-ρ region positions match, showing a remarkably fast sintering densification within this region. This causes the density fluctuation (SD) to decrease from the beginning of the sintering simulation. Then, the low-ρ region densify much more than the others at the end of the sintering. This causes a distortion on the surface (Fig. 14b), caused by localized large densification which leads to larger shrinkages within the low-ρ region.

The expectation is that longer sintering times would lead to the homogenization of the density within the components. However, the model demonstrates and predicts that components evolution during sintering would be different depending on the initial conditions from density and particle size distribution. Besides, predicted remarkable increases of the density heterogeneities within the powder components could cause cracks or instabilities during the sintering experiments. However, this model does not include any damage criteria to predict this consequence. In this line, further studies can be done to develop and integrate stress-dependent damage criteria on the sintering model for BJT components. This could be particularly useful to evaluate critical levels of heterogeneities within the green BJT components and select adequate sintering cycles for the materials and printing parameters used for manufacturing. Another idea from the present study consists of the implementation of BJT green properties into the continuum modeling of sintering. The initial properties proposed here (density and particle size distribution) can be obtained by experimental characterization. Also, these properties can be computed from simulation results of the BJT printing process by DEM [38,40,41]. By including simulation of each manufacturing step (printing and sintering), a digital twin for the manufacturing process can be developed. However, significant development efforts will be needed for more accurate simulation of the BJT printing and sintering process and the appropriate methodology to link these two models.

5. Conclusions

Microstructural heterogeneities in the as-printed samples produced by binder jetting technology (BJT) and its evolution during sintering stage were revealed for the first time using high-resolution synchrotron X-Ray computed tomography (SXCT). The ex-situ approach allows to follow the evolution during the standard industrial sintering (under H_2 atmosphere) of BJT stainless steel 316L components. The CT data collected allowed for the detailed characterization of the density distribution, particle size and pore morphological features evolution during the sintering process.

The relative density analysis showed a systematic fluctuation pattern along the building direction (Z axis) of 57 ± 1.6 %, with peaks separated by ~ 42 μm, equal to the layer thickness used during BJT printing of the components. In general, the initially complex interconnected porosity remains present during the heating stage until reaching sintering temperatures above 1300 °C. Increased densification caused by the greater diffusivity occurring due to the δ-ferrite phase transformation is responsible for the enhanced pore closure rate observed at sintering temperatures beyond 1300 °C. Finally, the pore network evolves into a configuration of distributed fine closed pores by the end of sintering after 60 min holding at 1370 °C. The peak separation of the density fluctuation pattern along the building direction decreased from ~ 42 μm (as printed) to ~ 33 μm (sintered for 60 min at 1370 °C), resulting in a final density of 99 ± 0.3 %. Density fluctuations were also detected along other directions orthogonal to the building direction, related to e.g. "cratering" effect potentially caused by the binder-powder interaction during the printing process. However, lower intensity and pattern consistency compared with the building direction was observed.

The fluctuating distribution of pore surface area along the vertical direction revealed slightly different kinetics of the sintering within diverse regions of the layered porosity. The sintering stress within the low- and high-density regions follows a quadratic evolution with the densification. The quadratic relationship of the calculated sintering stress evolution agrees with the equation used for the modelling of sintering.

The sintering model used is based on the linear-viscous case for free-sintering, including grain growth kinetics and effect of the δ-ferrite transformation during sintering of BJT 316L components. Simulation allowed to replicate the evolution of the density fluctuations observed by SXCT experiments with a mean error of 2 %. The initial standard deviation of the density fluctuation in as-printed samples was 1.6 % and decreased to ~ 0.5 % at the end of the sintering. Also, other extreme cases of density and particle size distribution were theoretically evaluated. The results showed that wider particle size distributions (1 μm to 130 μm) and severe particle segregation during printing could lead to a rapid increase of ~ 10 % on the initial density fluctuation during sintering. These relative density variations are undesirable and may result in final sintered part's defects including printed layer delamination, cracking, or excessive residual porosity. The introduced modeling approach opens the possibility for the prediction of these undesirable phenomena and can serve as a basis for an overall multistep BJT printing-sintering process optimization.

CRediT authorship contribution statement

Alberto Cabo Rios: Writing – original draft, Software, Investigation, Formal analysis, Conceptualization. **Tatiana Mishurova:** Writing – review & editing, Investigation, Conceptualization. **Laura Cordova:** Writing – review & editing, Investigation. **Mats Persson:** Writing – review & editing, Resources, Investigation. **Giovanni Bruno:** Writing – review & editing, Conceptualization. **Eugene Olevsky:** Writing – review & editing, Supervision, Software, Funding acquisition. **Eduard Hryha:** Writing – review & editing, Supervision, Funding acquisition, Conceptualization.

Declaration of competing interest

The authors declare that they have no known competing financial interests or personal relationships that could have appeared to influence the work reported in this paper.

Data availability

The data that has been used is confidential.

Acknowledgements

This work was conducted in the framework of the Centre for Additive Manufacturing – Metal (CAM^2), supported by the Swedish Governmental Agency of Innovation Systems (Vinnova). The support of the

National Science Foundation (Grant DMREF-2119832) is gratefully appreciated.

Appendix A

Since the samples designed for SXCT characterization are extremely small, they cannot be used for the characterization of shrinkages by using dilatometry measurements. Therefore, various cubical samples with dimensions of 10x10x10 mm^3 were printed together with the SXCT samples and were used for the characterization of the shrinkage and sintering behavior of the BJT samples. The sintering experiment for the full cycle (1370 °C / 60 min) was replicated as detailed in section 2.1. However, now the pushrod was in contact with the BJT cube's sample face so that the dimensional evolution during the sintering is measured. The same methodology developed in an earlier study [20] was used. Three different experiments were done by only varying the cube's orientation and, consequently, the axis aligned with the pushrod direction. Each experiment was performed to characterize the shrinkage along the X (binder deposition), Y (powder spreading) and Z (building direction) axis of the cube.

The sintering cycle used for the dilatometry experiments corresponds to the complete sintering cycle detailed in section 2.1, with a dwell temperature of 1370 °C and dwell time of 1 h. The measured sintering shrinkages along the different axes of the cubical sample are shown in Fig. 15. In general, the same shrinkage was observed along each direction during the heating step within temperatures below 1300 °C. Then, the shrinkage rate increases above 1300 °C and the shrinkages along different directions start to diverge until the end of sintering. This enhanced shrinkage rate is a consequence of the increased densification rate above 1300 °C attributed to the δ-ferrite formation. This phase transformation not only results on the increase on the volume diffusion from the BCC (δ ferrite) but also the multiplication of grain boundaries from the nucleation and growth of δ -ferrite grains along the austenite grain boundaries [20,21,33,35]. This same behavior has been many times observed previously during the sintering of stainless-steel powders [20,21,36,37,53–55]. Fig. 16 shows an EBSD phase map of the microstructure from the sintered cubical sample studied, the features discussed above can be seen. This microstructure consists of a matrix of austenite (FCC) grains, 3.2 % fraction of ferrite (BCC) grains preferentially located surrounding the austenite, and 1.3 % porosity. Also, high angle grain boundaries (>5°) are plotted, where 47.2 % of these boundaries were identified as twin boundaries.

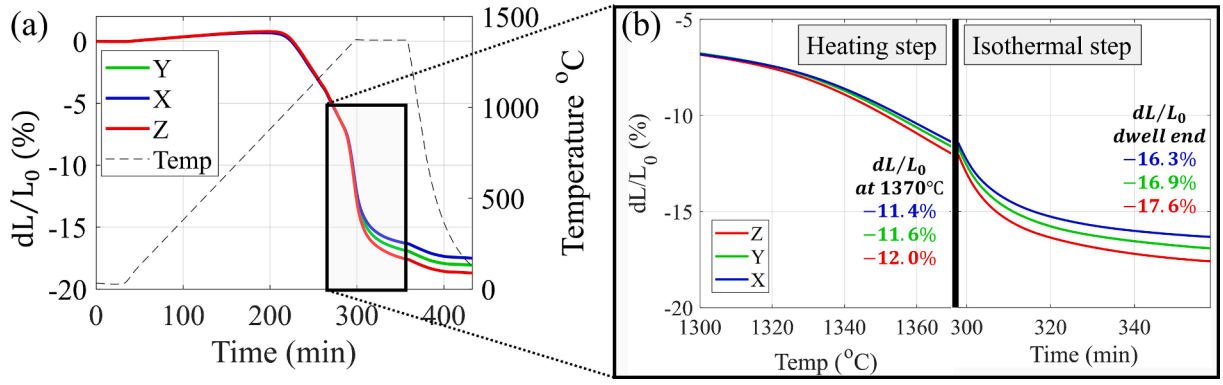

Fig. 15. Shrinkages evolution of the cubical samples subjected to dilatometry sintering experiments with the sample oriented along the different directions X (binder deposition), Y (powder spreading) and Z (building direction): (a) Complete data from dilatometry, (b) area zoom with plot of heating step (temperature vs. shrinkage) and isothermal step at 1370 °C (time vs. shrinkage).

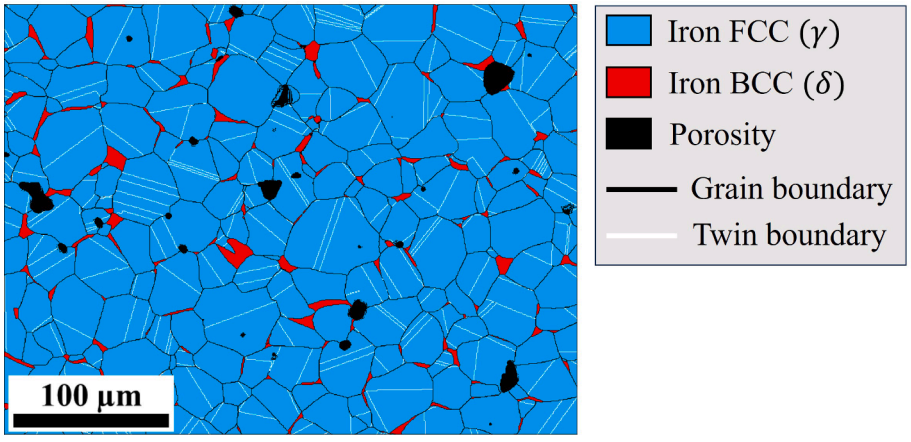

Fig. 16. EBSD phase map from the cubical sample sintered up to 1370 °C for 1 h, where FCC austenite (blue), BCC δ-ferrite (red) and porosity (black) phases are shown. The grain boundaries and twin boundaries are shown as black and white lines, respectively.

Note that the shrinkages anisotropy during sintering on the BJT samples in this study is minimal when compared with the typical anisotropy characterized in other studies [20,53,56–58]. Typically, the ratio between the shrinkage along the building direction and the other directions is typically between 1.13 and 1.3. However, this ratio is 1.07 and 1.04 between the shrinkages at the end of the isothermal step shown in Fig. 15(b). This minor anisotropy might be potentially related to the density fluctuations characterized by SXCT. During the last stage of the sintering cycle (specially during the dwell at 1370 °C), the shrinkages along different directions diverge (see Fig. 15) at the same time than the density fluctuations are drastically diminished (see Fig. 5 and Fig. 7). In conclusion, it can be argued that the progress of homogenization of the density distribution within BJT components is connected to the anisotropy on the external shrinkage along the different printing directions. However, the density distribution is most

likely not the only influence on the anisotropy of BJT components. Other factors like the particle size distribution anisotropy may have similar or greater impact on the evolution of the external dimensions.

Appendix B. Supplementary data

Supplementary data to this article can be found online at https://doi.org/10.1016/j.matdes.2024.112690.

References

[1] A. Mostafaei, E.L. Stevens, J.J. Ference, D.E. Schmidt, M. Chmielus, Binder jetting of a complex-shaped metal partial denture framework, Addit Manuf. 21 (2018) 63–68, https://doi.org/10.1016/j.addma.2018.02.014.

[2] G.J. Davies, S. Zhen, Metallic foams: their production, properties and applications, J Mater Sci. 18 (1983) 1899–1911, https://doi.org/10.1007/BF00554981.

[3] G.K. Meenashisundaram, Z. Xu, M.L.S. Nai, S. Lu, J.S. Ten, J. Wei, Binder jetting additive manufacturing of high porosity 316L stainless steel metal foams, Materials 13 (2020) 3744, https://doi.org/10.3390/MA13173744.

[4] B. Zhu, M. Duke, L.F. Dumée, A. Merenda, E. des Ligneris, L. Kong, P.D. Hodgson, S. Gray, Short review on porous metal membranes—Fabrication, commercial products, and applications, Membranes (basel) 8 (2018) 83, https://doi.org/10.3390/membranes8030083.

[5] P.S. Liu, K.M. Liang, Functional materials of porous metals made by P/M, electroplating and some other techniques, J Mater Sci. 36 (2001) 5059–5072, https://doi.org/10.1023/A:1012483920628.

[6] D. Ramakrishnan, Automotive applications of powder metallurgy, in: Advances in Powder Metallurgy: Properties, Processing and Applications, Woodhead Publishing, 2013, pp. 493–519, https://doi.org/10.1533/9780857098900.4.493.

[7] L. Nickels, AM and aerospace: An ideal combination, Met. Powder Rep. 70 (2015) 300–303, https://doi.org/10.1016/j.mprp.2015.06.005.

[8] A. Thompson, I. Maskery, R.K. Leach, X-ray computed tomography for additive manufacturing: a review, Meas Sci Technol. 27 (2016) 072001, https://doi.org/10.1088/0957-0233/27/7/072001.

[9] N.D. Parab, J.E. Barnes, C. Zhao, R.W. Cunningham, K. Fezzaa, A.D. Rollett, T. Sun, Real time observation of binder jetting printing process using high-speed X-ray imaging, Sci Rep. 9 (2019) 1–10, https://doi.org/10.1038/s41598-019-38862-7.

[10] S. Barui, H. Ding, Z. Wang, H. Zhao, S. Marathe, W. Mirihanage, B. Basu, B. Derby, Probing ink-powder interactions during 3D binder jet printing using time-resolved X-ray imaging, ACS Appl Mater Interfaces. 12 (2020) 34254–34264, https://doi.org/10.1021/acsami.0c03572.

[11] R.W. Penny, P.M. Praegla, M. Ochsenius, D. Oropeza, R. Weissbach, C. Meier, W. A. Wall, A.J. Hart, Spatial mapping of powder layer density for metal additive manufacturing via transmission X-ray imaging, Addit Manuf. 46 (2021) 102197, https://doi.org/10.1016/j.addma.2021.102197.

[12] G. Okuma, D. Kadowaki, T. Hondo, S. Tanaka, F. Wakai, Interface topology for distinguishing stages of sintering, Sci Rep. 7 (2017) 1–9, https://doi.org/10.1038/s41598-017-11667-2.

[13] G. Miao, M. Moghadasi, W. Du, Z. Pei, C. Ma, Experimental investigation on the effect of roller traverse and rotation speeds on ceramic binder jetting additive manufacturing, J Manuf Process. 79 (2022) 887–894, https://doi.org/10.1016/J.JMAPRO.2022.05.039.

[14] T. Dahmen, C.G. Klingaa, S. Baier-Stegmaier, A. Lapina, D.B. Pedersen, J.H. Hattel, Characterization of channels made by laser powder bed fusion and binder jetting using X-ray CT and image analysis, Addit Manuf. 36 (2020) 101445, https://doi.org/10.1016/j.addma.2020.101445.

[15] Y. Zhu, Z. Wu, W.D. Hartley, J.M. Sietins, C.B. Williams, H.Z. Yu, Unraveling pore evolution in post-processing of binder jetting materials: X-ray computed tomography, computer vision, and machine learning, Addit Manuf. 34 (2020) 101183, https://doi.org/10.1016/j.addma.2020.101183.

[16] A. Vagnon, O. Lame, D. Bouvard, M. Di Michiel, D. Bellet, G. Kapelski, Deformation of steel powder compacts during sintering: Correlation between macroscopic measurement and in situ microtomography analysis, Acta Mater. 54 (2006) 513–522, https://doi.org/10.1016/j.actamat.2005.09.030.

[17] O. Lame, D. Bellet, M. Di Michiel, D. Bouvard, In situ microtomography investigation of metal powder compacts during sintering, Nucl Instrum Methods Phys Res B. 200 (2003) 287–294, https://doi.org/10.1016/S0168-583X(02)01690-7.

[18] L. Chen, W. Chen, S. Zhang, S. Zou, T. Cheng, D. Zhu, Effect of bimodal powder on densification and mechanical properties of 316L stainless steel fabricated by binder jet 3D printing, J. Mater. Res. Technol. 27 (2023) 4043–4052, https://doi.org/10.1016/J.JMRT.2023.10.203.

[19] L. Chen, W. Chen, Z. Fu, G. Ding, Z. Chen, D. Zhu, Binder jet 3D printing of 316L stainless steel: orthogonal printing and sintering process optimization, Adv Eng Mater. (2022), https://doi.org/10.1002/adem.202200641.

[20] A. Cabo Rios, E. Hryha, E. Olevsky, P. Harlin, Sintering anisotropy of binder jetted 316L stainless steel: part I – sintering anisotropy, Powder Metall. 65 (2022) 273–282, https://doi.org/10.1080/00325899.2021.2020485.

[21] A. Cabo Rios, E. Hryha, E. Olevsky, P. Harlin, Sintering anisotropy of binder jetted 316L stainless steel: part II – microstructure evolution during sintering, Powder Metall. 65 (2022) 283–295, https://doi.org/10.1080/00325899.2021.2020486.

[22] T.T. Molla, D.W. Ni, R. Bulatova, R. Bjørk, C. Bahl, N. Pryds, H.L. Frandsen, Finite element modeling of camber evolution during sintering of bilayer structures, J. Am. Ceram. Soc. 97 (2014) 2965–2972, https://doi.org/10.1111/jace.13025.

[23] D. Giuntini, I.W. Chen, E. Olevsky, Sintering shape distortions controlled by interface roughness in powder composites, Scr Mater. 124 (2016) 38–41, https://doi.org/10.1016/j.scriptamat.2016.06.024.

[24] E. Olevsky, T.T. Molla, H.L. Frandsen, R. Bjørk, V. Esposito, D.W. Ni, A. Ilyina, N. Pryds, Sintering of multilayered porous structures: Part I-constitutive models, J. Am. Ceram. Soc. 96 (2013) 2657–2665, https://doi.org/10.1111/jace.12375.

[25] D.W. Ni, E. Olevsky, V. Esposito, T.T. Molla, S.P.V. Foghmoes, R. Bjørk, H. L. Frandsen, E. Aleksandrova, N. Pryds, Sintering of multilayered porous structures: Part II-experiments and model applications, J. Am. Ceram. Soc. 96 (2013) 2666–2673, https://doi.org/10.1111/jace.12374.

[26] E. Wheat, M. Vlasea, J. Hinebaugh, C. Metcalfe, Sinter structure analysis of titanium structures fabricated via binder jetting additive manufacturing, Mater Des. 156 (2018) 167–183, https://doi.org/10.1016/j.matdes.2018.06.038.

[27] A. Cabo Rios, E. Olevsky, E. Hryha, M. Persson, R.K. Bordia, Analytical models for initial and intermediate stages of sintering of additively manufactured stainless steel, Acta Mater. 249 (2023) 118822, https://doi.org/10.1016/j.actamat.2023.118822.

[28] C.R. Alberto, E.A. Olevsky, E. Hryha, M. Persson, Modelling of δ-ferrite transformation effect on the sintering behaviour of 316L binder jetted components, in: WorldPM 2022, EPMA, Lyon, France, 2022.

[29] A. Rack, S. Zabler, B.R. Müller, H. Riesemeier, G. Weidemann, A. Lange, J. Goebbels, M. Hentschel, W. Görner, High resolution synchrotron-based radiography and tomography using hard X-rays at the BAMline (BESSY II), Nucl Instrum Methods Phys Res A. 586 (2008) 327–344, https://doi.org/10.1016/j.nima.2007.11.020.

[30] H. Markötter, M. Sintschuk, R. Britzke, S. Dayani, G. Bruno, D. Bhattacharyya, Upgraded imaging capabilities at the BAMline (BESSY II), J Synchrotron Radiat. 29 (2022) 1292–1298, https://doi.org/10.1107/S1600577522007342.

[31] D. Gürsoy, F. De Carlo, X. Xiao, C. Jacobsen, TomoPy: A framework for the analysis of synchrotron tomographic data, J Synchrotron Radiat. 21 (2014) 1188–1193, https://doi.org/10.1107/S1600577514013939.

[32] Dragonfly 2020.2 [Computer software]. Object Research Systems (ORS) Inc, Montreal, Canada, 2020, (n.d.).

[33] Y. Wu, D. Blaine, B. Marx, C. Schlaefer, R.M. German, Sintering densification and microstructural evolution of injection molding grade 17–4 PH stainless steel powder, Metall Mater Trans A Phys Metall Mater Sci. 33 (2002) 2185–2194, https://doi.org/10.1007/s11661-002-0050-4.

[34] I.D. Jung, S. Ha, S.J. Park, D.C. Blaine, R. Bollina, R.M. German, Two-phase master sintering curve for 17–4 PH stainless steel, Metall Mater Trans A Phys Metall Mater Sci. 47 (2016) 5548–5556, https://doi.org/10.1007/s11661-016-3687-0.

[35] Y. Wu, R.M. German, D. Blaine, B. Marx, C. Schlaefer, Effects of residual carbon content on sintering shrinkage, microstructure and mechanical properties of injection molded 17–4 PH stainless steel, J Mater Sci. 37 (2002) 3573–3583, https://doi.org/10.1023/A:1016532418920.

[36] B. Berginc, Z. Kampus, B. Sustarsic, Influence of feedstock characteristics and process parameters on properties of MIM parts made of 316L, Powder Metall. 50 (2007) 172–183, https://doi.org/10.1179/174329007X164862.

[37] S. Mirzababaei, S. Pasebani, A Review on Binder Jet Additive Manufacturing of 316L Stainless Steel, Journal of Manufacturing and Materials Processing. 3 (2019) 82, https://doi.org/10.3390/jmmp3030082.

[38] M. Li, G. Miao, W. Du, Z. Pei, C. Ma, Difference between powder bed density and green density for a free-flowing powder in binder jetting additive manufacturing, J Manuf Process. 84 (2022) 448–456, https://doi.org/10.1016/j.jmapro.2022.10.030.

[39] L.C. Capozzi, A. Sivo, E. Bassini, Powder spreading and spreadability in the additive manufacturing of metallic materials: a critical review, J Mater Process Technol. 308 (2022) 117706, https://doi.org/10.1016/j.jmatprotec.2022.117706.

[40] G. Miao, W. Du, Z. Pei, C. Ma, A literature review on powder spreading in additive manufacturing, Addit Manuf. 58 (2022) 103029, https://doi.org/10.1016/j.addma.2022.103029.

[41] Y. Lee, P. Nandwana, S. Simunovic, Powder spreading, densification, and part deformation in binder jetting additive manufacturing, Progress in Additive Manufacturing. (2021), https://doi.org/10.1007/s40964-021-00214-1.

[42] F. Wakai, Y. Shinoda, T. Akatsu, Methods to calculate sintering stress of porous materials in equilibrium, Acta Mater. 52 (2004) 5621–5631, https://doi.org/10.1016/j.actamat.2004.08.021.

[43] G. Okuma, D. Kadowaki, T. Hondo, A. Sato, S. Tanaka, F. Wakai, Computation of sintering stress and bulk viscosity from microtomographic images in viscous sintering of glass particles, J. Am. Ceram. Soc. 100 (2017) 867–875, https://doi.org/10.1111/jace.14609.

[44] R.M. German, Sintering trajectories: description on how density surface area, and grain size change, Jom. 68 (2016) 878–884, https://doi.org/10.1007/s11837-015-1795-8.

[45] E.A. Olevsky, Theory of sintering: from discrete to continuum, Mater. Sci. Eng. R. Rep. 23 (1998) 41–100, https://doi.org/10.1016/S0927-796X(98)00009-6.

[46] C. Manière, S. Chan, G. Lee, J. McKittrick, E.A. Olevsky, Sintering dilatometry based grain growth assessment, Results Phys. 10 (2018) 91–93, https://doi.org/10.1016/j.rinp.2018.05.014.
[47] G. Kerbart, C. Manière, C. Harnois, S. Marinel, Predicting final stage sintering grain growth affected by porosity, Appl Mater Today. 20 (2020), https://doi.org/10.1016/j.apmt.2020.100759.
[48] E.A. Olevsky, C. Garcia-Cardona, W.L. Bradbury, C.D. Haines, D.G. Martin, D. Kapoor, Fundamental aspects of spark plasma sintering: II. Finite element analysis of scalability, J. Am. Ceram. Soc. 95 (2012) 2414–2422, https://doi.org/10.1111/j.1551-2916.2012.05096.x.
[49] E. Olevsky, A. Molinari, Instability of sintering of porous bodies, Int J Plast. 16 (2000) 1–37, https://doi.org/10.1016/S0749-6419(99)00032-7.
[50] R.K. Bordia, S.J.L. Kang, E.A. Olevsky, Current understanding and future research directions at the onset of the next century of sintering science and technology, J. Am. Ceram. Soc. 100 (2017) 2314–2352, https://doi.org/10.1111/jace.14919.
[51] D.J. Green, O. Guillon, J. Rödel, Constrained sintering: A delicate balance of scales, J Eur Ceram Soc. 28 (2008) 1451–1466, https://doi.org/10.1016/j.jeurceramsoc.2007.12.012.
[52] H.L. Frandsen, E. Olevsky, T.T. Molla, V. Esposito, R. Bjørk, N. Pryds, Modeling sintering of multilayers under influence of gravity, J. Am. Ceram. Soc. 96 (2013) 80–89, https://doi.org/10.1111/jace.12070.
[53] N. Lecis, M. Mariani, R. Beltrami, L. Emanuelli, R. Casati, M. Vedani, A. Molinari, Effects of process parameters, debinding and sintering on the microstructure of 316L stainless steel produced by binder jetting, Mater. Sci. Eng. A 828 (2021) 142108, https://doi.org/10.1016/j.msea.2021.142108.
[54] R. Batmaz, A. Zardoshtian, T.D. Sabiston, R. Tangestani, A. Chakraborty, N. Krutz, S. Pendurti, A. Natarajan, E. Martin, An Investigation into Sinterability Improvements of 316L Binder Jet Printed Parts, Metall Mater Trans A Phys Metall Mater Sci. 53 (2022) 915–926, https://doi.org/10.1007/s11661-021-06564-3.
[55] J. Song, T. Barriere, B. Liu, J.C. Gelin, G. Michel, Experimental and numerical analysis on sintering behaviours of injection moulded components in 316L stainless steel powder, Powder Metall. 53 (2010) 295–304, https://doi.org/10.1179/003258908X334212.
[56] B. Barthel, S.B. Hein, C. Aumund-Kopp, F. Petzoldt, Influence of Particle Size Distribution in Metal Ber Jetting – Effects on the Properties of Green and Sintered Parts. In: Procedia EuroPM 2019: International Powder Metallurgy Congress and Exhibition, 2019.
[57] A. Mostafaei, P. Rodriguez De Vecchis, I. Nettleship, M. Chmielus, Effect of powder size distribution on densification and microstructural evolution of binder-jet 3D-printed alloy 625, Mater Des. 162 (2019) 375–383, https://doi.org/10.1016/j.matdes.2018.11.051.
[58] D. Huber, L. Vogel, A. Fischer, The effects of sintering temperature and hold time on densification, mechanical properties and microstructural characteristics of binder jet 3D printed 17–4 PH stainless steel, Addit Manuf. 46 (2021) 102114, https://doi.org/10.1016/j.addma.2021.102114.